

Magmatism Associated with Orogenic Collapse of the Betic–Alboran Domain, SE Spain

S. P. TURNER^{1*}, J. P. PLATT², R. M. M. GEORGE¹, S. P. KELLEY¹,
D. G. PEARSON³ AND G. M. NOWELL³

¹DEPARTMENT OF EARTH SCIENCES, THE OPEN UNIVERSITY, WALTON HALL, MILTON KEYNES MK7 6AA, UK

²DEPARTMENT OF GEOLOGY, UNIVERSITY COLLEGE LONDON, GOWER STREET, LONDON WC1E 6BT, UK

³DEPARTMENT OF GEOLOGY, UNIVERSITY OF DURHAM, SOUTH ROAD, DURHAM DH1 3LE, UK

RECEIVED APRIL 5, 1998; REVISED TYPESCRIPT ACCEPTED JANUARY 8, 1999

Extensional collapse of the Betic–Alboran Domain in the Miocene was accompanied by several discrete episodes of magmatism which provide insights into the relationships between the thermal and mechanical state of the lithosphere during late orogenesis. The tholeiitic Malaga dykes, emplaced at ~30–27 Ma, have flat rare earth element (REE) patterns and low $^{87}\text{Sr}/^{86}\text{Sr}$ and high $^{143}\text{Nd}/^{144}\text{Nd}$ indicative of shallow decompression melting (5–15%) within the asthenosphere following removal of lithospheric mantle. Calc-alkaline magmas, erupted between 15 and 6 Ma, have negative Ta–Nb and Ti anomalies, elevated $^{87}\text{Sr}/^{86}\text{Sr}$ and low $^{143}\text{Nd}/^{144}\text{Nd}$, and represent increasing degrees of crustal contamination (20–50%) of rising asthenospheric magmas. The end of this phase of volcanism was marked by emplacement of crustally derived cordierite–garnet dacites suggesting very high Moho temperatures. Emplacement of alkali basalts at 10 Ma, which have smooth, convex-up, incompatible element patterns and low $^{87}\text{Sr}/^{86}\text{Sr}$ and high $^{143}\text{Nd}/^{144}\text{Nd}$, is interpreted to reflect partial melting within the lower lithosphere. These lavas were succeeded by lamproites at 7 Ma, which have very high $^{87}\text{Sr}/^{86}\text{Sr}$ and low $^{143}\text{Nd}/^{144}\text{Nd}$, negative Ta–Nb, Ti and Eu anomalies and extreme light REE enrichment. These formed by partial melting, in the presence of residual phlogopite, which buffered K and Nb concentrations, of shallow lithospheric mantle which had been enriched by 2–3% of a sediment component. The temporal sequence from the alkali basalts to the lamproites is interpreted to record the vertical progression of partial melting through the Iberian lithospheric mantle remaining at the margins of the Alboran Sea as convective removal propagated outwards in the orogen. The general cessation of magmatism at around 6 Ma presumably reflects thermal rethickening of the

lithospheric mantle. Overall, the magmatic succession is more consistent with a geodynamic model involving convective removal of the majority of the lithospheric mantle than with models invoking wholesale delamination at the Moho, slab detachment or slab roll-back.

KEY WORDS: Betic–Alboran Domain; magmatism; geochemistry; orogenic collapse; convective removal

INTRODUCTION

The geodynamic processes responsible for the cessation of contractional deformation and the onset of extensional collapse in the Betic–Alboran Domain are the subject of much interest and the relative roles of slab roll-back, slab detachment, delamination and convective thinning of the lithospheric mantle remain hotly debated. This paper investigates the petrogenesis of the associated post-contractional magmatic rocks which display marked temporal changes in composition indicative of changes in magma source regions. The aim is to integrate these with the structural and metamorphic history of the orogen in order to track the evolving relationship between the thermal and mechanical state of the lithosphere during late orogenesis and extensional collapse. Such constraints

*Corresponding author. Telephone: +44 1908 652643. Fax: +44 1908 655151. e-mail: s.p.turner@open.ac.uk

should, in principle, be able to discriminate between the various competing geodynamic models.

THE BETIC CORDILLERA AND THE ALBORAN DOMAIN

The Alboran Sea in the westernmost Mediterranean is one of the clearest examples of a marine basin that has formed by late-orogenic extension on the site of an earlier contractional orogen characterized by thick crust (Platt & Vissers, 1989). The remains of this orogen are preserved in the Internal Zones of the mountain chains that surround the Alboran Sea to the north, west and south (Fig. 1): the Betic Cordillera of southern Spain and the Rif of Morocco (García-Dueñas *et al.*, 1992). It has also been sampled by the Ocean Drilling Program (ODP) at Site 976 in the Alboran Sea (Comas *et al.*, 1996; Platt *et al.*, 1996). The orogen developed during Late Cretaceous (?) and Early Tertiary time, presumably as a result of the convergence between Africa and Iberia. It is characterized by metamorphic rocks that record pressures up to 1.5 GPa, suggesting that the orogenic crust reached a thickness of 50 km or more [see Vissers *et al.* (1995) for review]. During the early Miocene, however, this orogen underwent an extraordinarily rapid phase of extension, resulting in the exhumation of deep-seated metamorphic rocks and the underlying mantle (the Ronda and Beni Bousera peridotites) on time-scales of a few million years (Monié *et al.*, 1994), and thinning of the crust to 15–20 km under the Alboran Sea (e.g. Banda *et al.*, 1983). Extension in the Alboran Domain took place in the context of continuing N–S to NW–SE convergence of the African and Iberian plates, and these motions were accommodated by shortening in the peripheral Betic and Rif fold-and-thrust belts, which define the Gibraltar arc (Platzman, 1992). During this process, the margins of the Alboran Domain were emplaced onto African and Iberian continental crust, which is why they are emergent at the present day (Vissers *et al.*, 1995).

The Alboran region shows a number of distinctive features that may bear on the geodynamic causes of the Miocene phase of extension:

(1) seismological evidence (Seber *et al.*, 1996), supported by heat flow data (Polyak *et al.*, 1996), suggests that the Alboran Sea is underlain by abnormally hot mantle at shallow depths; and the presence of one or more detached bodies of relatively cold mantle at depths of up to 600 km is suggested by seismic tomography (Blanco & Spakman, 1993) and seismicity (Grimison & Chen, 1986; Seber *et al.*, 1996).

(2) Extension resulted in the exhumation of the Ronda and Beni Bousera peridotite bodies (Fig. 1). Van der Wal & Vissers (1993) inferred a two-stage exhumation history for these rocks. Stage 1 may have occurred during the

Triassic–Jurassic rifting of Iberia from Africa, stretching the lithosphere, and bringing the peridotites from the diamond stability field up to about 70 km depth, where they re-equilibrated thoroughly in the spinel field and cooled to 900°C or less, becoming incorporated into the Mesozoic lithosphere. Exhumation from 70 km to crustal depths probably occurred in the late Oligocene and early Miocene, and was associated with substantial heating (to about 1100°C) during decompression into the plagioclase field.

(3) Thermobarometric data on high-grade metamorphic rocks surrounding the Ronda peridotite (Argles *et al.*, 1999), and high-grade rocks sampled from beneath the Alboran Sea itself (Platt *et al.*, 1996, 1998; Soto & Platt, 1999), all suggest that decompression was accompanied by heating from an external source.

(4) Extension in the Alboran Domain was accompanied by mixed mode volcanism distributed over a large region, without any obvious concentration or orientation of centres (Bellon *et al.*, 1983; Comas *et al.*, 1999).

(5) Coeval shortening in the external Betic–Rif arc shows a strong westward component, swinging from NW to WNW in the external Betics (Guezou *et al.*, 1991; Lonergan *et al.*, 1994; Platt *et al.*, 1995; Kirker & Platt, 1998) to W, SW, and S in the Rif (Platzman *et al.*, 1993). Thrusting was accompanied by large vertical-axis rotations, clockwise in the Betics (Platzman, 1992; Allerton *et al.*, 1993; Platt *et al.*, 1995) and anticlockwise in the Rif (Platzman *et al.*, 1993). This pattern of thrusting and vertical axis rotation suggests a significant westward motion of the Alboran Domain with respect to the surrounding continents during the extensional event.

COMPETING GEODYNAMIC MODELS

There are currently several competing hypotheses to explain the Miocene phase of extension that created the Alboran Sea basin:

(1) back-arc extension may have been driven by the retreat of a subduction zone on the western margin of the Alboran Domain. The subduction zone is thought to have retreated westwards during the course of the Miocene from somewhere within the western Mediterranean, either to the present position of the Gibraltar arc (Lonergan & White, 1997), or to the Horseshoe Seamounts in the eastern Atlantic (Royden, 1993).

(2) Extension was a result of delamination of the lithospheric mantle from beneath the crust of the Alboran Domain. García-Dueñas *et al.* (1992) suggested that the delaminated mantle slab peeled off towards the west, whereas Docherty & Banda (1995) suggested that it peeled off towards the east.

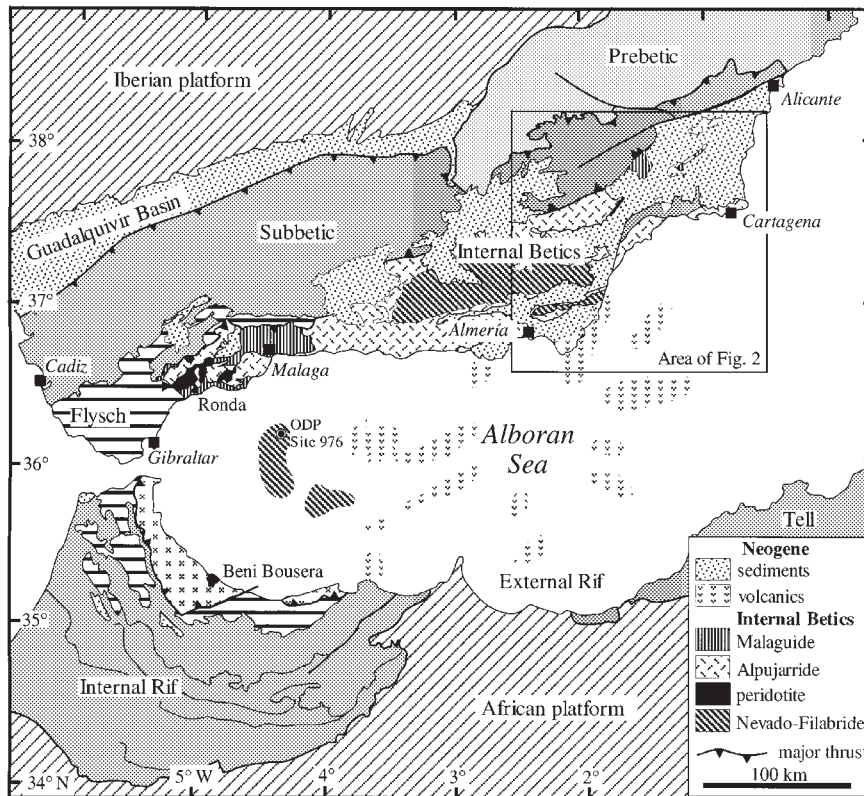


Fig. 1. Map of the Alboran Domain showing locations and ages of magmatic rocks associated with extensional collapse [modified from Platt & Vissers (1989) and Vissers *et al.* (1995)]. The E–W trending Malaga dyke swarm crops out ~150 km to the north of Malaga. The volcanic rocks indicated beneath the Alboran Sea are known from dredging and submersible sampling. Seismic data suggest that these volcanic rocks are fairly continuous beneath Messinian–Recent sediment, up to 1000 m thick, over the intervening areas. ODP Site 976 intersected high-grade metamorphic rocks beneath the Alboran Sea (Platt *et al.*, 1996, 1998). The area of Fig. 2 is outlined.

(3) Extension was a consequence of the convective removal of the lower part of the conductive thermal boundary layer beneath a region of thickened crust and lithosphere produced by pre-Miocene convergence between Africa and Iberia (Platt & Vissers, 1989).

(4) Extension was driven by the detachment of a subducting lithospheric slab beneath the convergent orogen (Carminati *et al.*, 1998).

All of the explanations outlined above depend on postulates about the behaviour of the mantle lithosphere in regions of continental collision, none of which is easy to measure or observe directly. Devising effective tests to distinguish among them is therefore difficult, particularly when the processes involved took place at some time in the geological past. However, it may be possible to distinguish among the hypotheses using the geometry and evolution of the pattern of magmatism, uplift and deformation that they produce. The case for a retreating subduction zone has been based partly on the relative westward motion of the Alboran domain suggested by the kinematics of thrusting and the pattern of vertical axis rotations in the peripheral thrust belt, for example

(Lonergan & White, 1997). On the other hand, this explanation would also predict a westward migrating volcanic arc, which is not apparent. Docherty & Banda (1995) suggested that eastward younging of extension and subsidence in the Alboran Sea support an eastward propagation of mantle delamination beneath the region. This idea was based on a mis-identification of the acoustic basement beneath Pliocene sediments in seismic profiles across the eastern Alboran Basin, however: Docherty & Banda (1995) considered the acoustic basement to be the floor of the basin, whereas it is in fact composed of Miocene volcanic rocks of comparable age to the sedimentary basin fill in the western Alboran basin (Comas *et al.*, 1999).

Delamination, convective removal of lithosphere and slab detachment all predict significant uplift before the onset of extension, together with decompressional magmatism and transient conductive heating of the lithosphere (Platt & England, 1994). The surface geometry and evolution of the effects should differ according to the model, but the differences may not be sufficiently clearcut to be diagnostic. In fact, the differences among

these three models may reflect more the differing prejudices of their proponents about the mechanical state of the subcontinental lithosphere than any real difference in the physics of the process—a point discussed elegantly by Houseman (1996).

The most clearcut difference in opinion lies between those who argue for extension driven by forces applied at an adjacent convergent plate boundary, as in the retreating subduction zone model, and those who call on forces generated locally by processes in the immediately subjacent lithosphere. These two classes of models predict significantly differing thermal structures at depth, and hence different styles and locations of magmatism, as well as different thermal effects during metamorphism. Argles *et al.* (1999), Platt *et al.* (1998) and Soto & Platt (1999) have addressed the question of the metamorphism, and make the case for the removal of much or all of the Alboran lithosphere to provide sufficient input of heat during decompression.

MAGMATIC HISTORY OF THE AREA AND SAMPLE SELECTION

Neogene magmatic activity associated with collapse of the Betic orogen is observed in the Alboran Sea as well as in the Betic and Rif thrust belts. In the following discussion sample numbers refer to those collected for this study, the localities for which are shown schematically in Figs 1 and 2 (longitudes and latitudes are given in the geochemical data tables). The magmatic rocks can be subdivided into several subgroups as follows.

The earliest manifestation of magmatism associated with extension is the intrusion of an extensive (~1000 km²), east–west trending, tholeiitic dyke swarm in the internal Betic zone north of Malaga (Fig. 1). As discussed by Torres-Roldán *et al.* (1986), these dykes are fine-grained, porphyritic to sub-ophitic plagioclase–hornblende diorites containing subordinate amounts of clinopyroxene or interstitial quartz and rarer biotite. Early K–Ar ages suggested that the dykes were intruded in the early Miocene around 22–23 Ma (Torres-Roldán *et al.*, 1986). We collected both hand specimens (samples B322, B323) and palaeomagnetic drill cores (samples M1–M11) from the dyke swarm.

Subsequently, widespread calc-alkaline volcanic activity occurred in the Alboran Sea region and along the SE coastal margin of the Betics, adjacent to the Alboran Sea (Figs 1 and 2). Volcanism in the region around Mazarrón (samples B301–303) produced amphibole ± biotite bearing andesites, dacites and rhyolites, and K–Ar ages of 6.8 and 7.2 Ma have been reported from similar outcrops slightly further east, near Cartagena (Bellon *et al.*, 1983). Bellon *et al.* (1983) obtained a K–Ar age range of 15.2–7.9 Ma for voluminous calc-alkaline lavas which

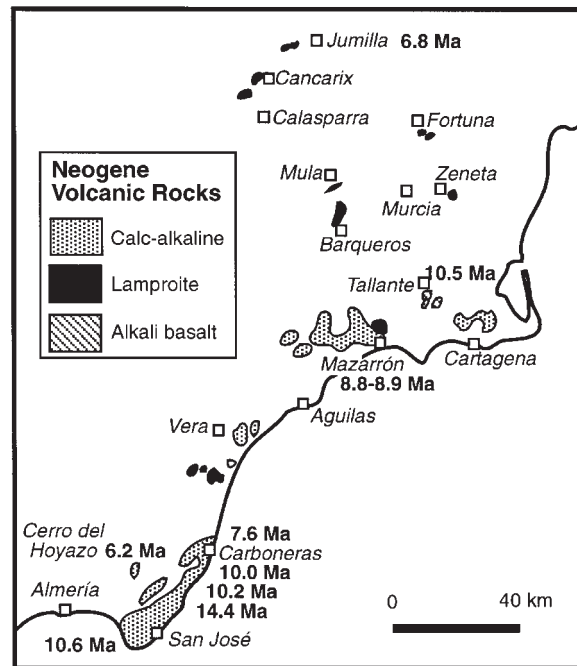


Fig. 2. Map showing locations and new ⁴⁰Ar/³⁹Ar ages for Neogene calc-alkaline and lamproitic magmatic rocks in SE Spain [modified from Venturelli *et al.* (1984)]. It should be noted that the lamproites and alkali basalts crop out inland of the calc-alkaline volcanic rocks which extend beneath the Alboran Sea (see Fig. 1).

form a 1000 m section in the Cabo de Gata area (Fig. 2), which Di Battistini *et al.* (1987) subsequently divided into 12–9 Ma amphibole ± biotite bearing andesites, dacites and rhyolites stratigraphically overlain by pyroxene-phyric bearing andesites, dacites and rhyolites which were erupted around 8 Ma. We collected a representative selection of samples from the Cabo de Gata (B309–320). Finally, sample B321 is an example of the rare cordierite–garnet-bearing andesites and dacites which were erupted at Cerro del Hoyazo as well as several other nearby localities (Fig. 2). Detailed work by Munksgaard (1984) suggests that these rocks formed by anatexis of semi-pelitic source rocks and therefore may be representative of local crustal melts.

Phlogopite-bearing alkalic basalts and trachybasalts form several eroded cinder-cones northwest of Cartagena, such as Cabezo de Tallante (Fig. 2). These consist of fine-grained to glassy basaltic scoria (samples B304 scoria and B304 host) and contain rare hornblende–clinopyroxene cumulate nodules (sample B304 hb) and more numerous spinel peridotite xenoliths (samples S1, S3 and S4) which were previously documented by Ancochea & Nixon (1987). The lavas have previously yielded K–Ar ages of 2.6 and 2.8 Ma (Bellon *et al.*, 1983).

Finally, to the north of Tallante and the calc-alkaline suites, a series of ultrapotassic lamproites were emplaced

Table 1: New ^{40}Ar – ^{39}Ar ages for Betic volcanics

Sample	Locality	Ma	$\pm 1\sigma$
<i>Malaga dyke</i>			
M7B-4	Malaga	17.7	0.6
M7A-7	Malaga	30.2	0.9
<i>Calc-alkaline volcanics</i>			
B318	Los Escuilos	14.4	0.6
B320	Rambla de Morales	10.6	0.6
B312	Road to Las Negras	10.2	1.2
B311	Cabo de Gata	10.0	1.8
B303	Mazarrón	8.9	0.6
B301	Mazarrón	8.8	0.2
B309	Garrucha–Carboneras Road	7.6	0.2
B321	Cordierite dacite	6.2	0.4
<i>Alkali basalt</i>			
B304	Tallante volcano	10.5	0.6
<i>Lamproite</i>			
B305	Jumilla	6.8	0.4

in the eastern Betic Cordillera along a NNE trend extending from Vera to Jumilla (Fig. 2). This magmatism occurred after the end of the extensional event and the emplacement of the Alboran Domain onto the Iberian continental margin. These rocks are fine-grained, Mg-rich olivine–phlogopite-bearing rocks containing subordinate amounts of pyroxene, sanidine, apatite and sometimes leucite. Some of these lamproites also contain spinel lherzolite xenoliths (Ancochea & Nixon, 1987). Previous K–Ar ages for several lamproites from Barqueros, Fortuna and Cancarix ranged from 5.7 to 7 Ma (Bellon *et al.*, 1983). Analytical data for these rocks were previously presented by Venturelli *et al.* (1984, 1988) and Nelson *et al.* (1986), and here we provide data on new samples from the Jumilla (samples B305 and B305a), Cancarix (sample B306) and Vera (sample B307) outcrops (Fig. 2).

ANALYTICAL TECHNIQUES

Thirty-nine samples were selected to encompass the compositional, spatial and temporal range of magmatism in the Betics. Following removal of weathered surfaces and sectioning, samples were crushed in a steel jaw-crusher, following which several grains of hornblende and biotite were extracted from selected samples for $^{40}\text{Ar}/^{39}\text{Ar}$ dating; elsewhere whole-rock chips were hand picked for dating purposes. The remaining material was milled in an agate mortar. The whole-rock and mineral $^{40}\text{Ar}/^{39}\text{Ar}$ isotope analyses in Table 1 were performed

either by IR laser spot analysis or by IR laser stepped heating using an MAP 215-50 mass spectrometer and following techniques outlined by Kelley (1995). Major and trace element data on 39 samples were analysed by X-ray fluorescence (XRF) on fused discs and pressed pellets, respectively, following standard techniques at the Open University (Potts *et al.*, 1984). A subset of 17 volcanic samples, as well as three spinel lherzolite xenoliths from Tallante volcano, were selected for more detailed investigation. For these samples, trace element data were determined by inductively coupled plasma mass spectrometry (ICP-MS) in Durham. Powders were dissolved using a standard HF–HNO₃ technique, care being taken to ensure no fluoride residue. Samples were spiked with Rh, In and Bi before dilution to 3.5% HNO₃ to monitor internal drift, and the resulting solutions analysed on a Perkin–Elmer–SCIEX Elan 6000 inductively coupled plasma mass spectrometer using a cross-flow nebulizer. Oxide interferences for most analyses were substantially less than 2.5% of the total signal. Appropriate corrections were made using oxide/metal ratios measured on matrix-matched standard solutions. Calibration was achieved using matrix-matched international and in-house reference materials. Total procedural blanks for all elements were negligible for all analyses. Reproducibility, based on replicate digestions of standards and samples, varied from 1.5% to 3% for most analyses. This same subset of samples was analysed for Sr, Nd and Pb isotopes at the Open University. Following dissolution using a standard HF–HNO₃ technique, Sr and rare earth element (REE) fractions were separated using cationic ion-exchange resin following which Nd was purified using hydrogen-diethyl-hexyl-phosphate (HDEHP) (Richard *et al.*, 1976). Separation of Pb was achieved using a small-scale anionic ion-exchange technique similar to that of Mahnes *et al.* (1978). Isotope ratios were determined in static multi-collector mode on either a Finnigan MAT 261 or 262. Sr was fractionation corrected to $^{86}\text{Sr}/^{88}\text{Sr} = 0.1194$ and Nd to $^{144}\text{Nd}/^{146}\text{Nd} = 0.7219$, and the resultant isotope ratios were normalized with respect to internally determined values for $^{86}\text{Sr}/^{88}\text{Sr}$ in NBS 987 = 0.710220 (± 18) and $^{144}\text{Nd}/^{146}\text{Nd}$ in Johnson & Matthey Nd = 0.511778 (± 12). Pb was analysed in temperature-controlled runs (1250°C), and the ratios were corrected for ~1‰ per atomic mass unit mass-fractionation using our values for NBS 981: $^{206}\text{Pb}/^{204}\text{Pb} = 16.932$ (± 2), $^{207}\text{Pb}/^{204}\text{Pb} = 15.485$ (± 2), $^{208}\text{Pb}/^{204}\text{Pb} = 36.686$ (± 2). Quoted errors are 1 SD, and errors on individual runs are significantly less than the quoted reproducibility. Blanks for Sr, Nd and Pb during the period of analysis were typically <1 ng, 200 pg and 300 pg, respectively. For plotting on diagrams, the Sr and Nd isotope ratios were age corrected to 30 Ma in the case of the Malaga dykes, 10 Ma for Tallante, 7 Ma for the lamproites and 8 Ma for the calc-alkaline volcanic rocks, excepting where

individual ages have been determined, in which case the age quoted in Table 1 was used.

RESULTS

The new $^{40}\text{Ar}/^{39}\text{Ar}$ age data are presented in Table 1 and the full Ar isotope data are listed in the Appendix (Table A1). The major element, ICP-MS trace element, and Sr, Nd and Pb isotope data for the 17 representative samples are presented in Table 2 and the XRF data for the remaining 19 samples are given in the Appendix (Table A2). Table 3 contains the analyses for the three spinel lherzolite xenoliths from Tallante.

New laser $^{40}\text{Ar}/^{39}\text{Ar}$ geochronological data

The $^{40}\text{Ar}/^{39}\text{Ar}$ age data are shown in relation to their position in Fig. 2 (the Malaga dyke swarm lies to the north of Malaga in Fig. 1). The $^{40}\text{Ar}/^{39}\text{Ar}$ data for the Malaga dykes are the most complex of all samples analysed and the ages reported here (Fig. 3) resulted from a larger study which produced scattered ages within the range of the two samples in Table 1. Many samples have been affected by fluid ingress and although the two samples shown in Fig. 3 exhibit noisy plateaux, they also exhibit alteration in thin section. Sample M7B-4 (Fig. 3a and b) yielded a sub-plateau range over the first 70% of release plateau, though it was noisy. An isochron of these data yielded an age of 17.7 ± 0.6 Ma. Higher temperature release yielded increased $^{37}\text{Ar}/^{39}\text{Ar}$ ratios resulting from release of argon from plagioclase and scattered ages. Plagioclase is extensively altered in thin section. The other sample, M7A-7 (Fig. 3c and d) yielded high and variable initial ages, followed by a central plateau of around 80% release and an upper 10% of slightly older ages. In this case, however, the initial ages were accompanied by higher $^{37}\text{Ar}/^{39}\text{Ar}$ ratios, probably resulting from carbonate contamination. Other samples from the same area produced similar variations though none produced reproducible ages. The two samples shown here both contained small amounts of biotite and it is likely that the plateau sections in both analyses were dominated by argon release from biotite.

The two ages produced (30.2 ± 0.9 Ma and 17.7 ± 0.6 Ma) reflect partial alteration, with the younger age reflecting metamorphic ages of 17–22 Ma, which are common elsewhere in the Betics (Priem *et al.*, 1979; Monié *et al.*, 1994; Kelley & Platt, 1999). The older age, 30.2 Ma, is close to the time suggested for lithospheric removal (i.e. 27 Ma, Platt & Vissers, 1989; Platt *et al.*, 1998) and may represent the best estimate for the true intrusion age of these dykes. Earlier K–Ar ages of 22–23 Ma for these dykes (Torres-Roldán *et al.*, 1986) coincide with the age of the thermal overprint in the crustal rocks.

Further work is under way to constrain the relative ages of the intrusions and the thermal overprint.

Two biotite separates from the calc-alkaline volcanic rocks in the Mazarrón region (samples B301–303) yielded a narrow range of Ar–Ar ages of 8.8–8.9 Ma, slightly older than previously reported K–Ar ages of 6.8 and 7.2 Ma (Bellon *et al.*, 1983) though the Ar–Ar samples were obviously derived from a small database. Six samples from the Cabo de Gata (B309–320) area yielded $^{40}\text{Ar}/^{39}\text{Ar}$ ages of 14.4–7.2 Ma, similar to the range in K–Ar ages reported by Bellon *et al.* (1983) and Di Battistini *et al.* (1987). Four biotite separates, two amphibole separates and two whole-rock samples were analysed by total fusion of individual grains. Although it has not been possible to check the ages directly against stratigraphy and previous K–Ar ages, the lack of any correlation between rock type, mineral separate and age indicates that the apparent age range reflects a true span of volcanism. Finally, the cordierite–garnet dacite (sample B321) gave an $^{40}\text{Ar}/^{39}\text{Ar}$ biotite age of 6.2 ± 0.4 Ma.

Phlogopites from an alkalic basalt from Tallante were analysed by total laser fusion resulting in an age of 10.5 ± 0.6 Ma. However, previous K–Ar whole-rock determinations of 2.7 ± 0.3 and 2.8 ± 0.3 Ma (Bellon *et al.*, 1983) from the same area appear to contradict this age. The earlier K–Ar analyses were performed on whole-rock material yielding low concentrations of radiogenic argon (11–23% $^{40}\text{Ar}^*$) whereas the $^{40}\text{Ar}/^{39}\text{Ar}$ analyses were 70–80% radiogenic. It may be that the phlogopites contain high concentrations of excess argon though the ages were reproducible despite variations in radiogenic contents. However, it seems more likely, given the low K contents of the whole rock compared with the phlogopite phenocrysts, that the older $^{40}\text{Ar}/^{39}\text{Ar}$ age of 10.5 ± 0.6 Ma is the more reliable.

Finally, the $^{40}\text{Ar}/^{39}\text{Ar}$ total fusion whole-rock age of 6.8 ± 0.4 Ma obtained for a lamproite sample from Jumilla is consistent with previous K–Ar ages for several lamproites from Barqueros, Fortuna and Cancarix, which ranged from 5.7 to 7 Ma (Bellon *et al.*, 1983).

Major elements and compatible trace elements

Selected major element data are shown in SiO_2 -variation diagrams in Fig. 4. The Malaga dykes display a limited compositional variation and cluster on most diagrams. They are moderately magnesian ($\text{MgO} = 4.1\text{--}7.4$) with 51.6–56.7% SiO_2 and have *mg*-numbers ranging from 46 to 64 [where *mg*-number = molecular $\text{Mg}/(\text{Mg} + \text{Fe}_{\text{total}})$]. K_2O contents are <1% (Fig. 4d) and they record a tholeiitic crystallization history that involved moderate Fe enrichment (Torres-Roldán *et al.*, 1986). Concentrations of compatible trace elements, such as Cr,

Table 2: Analyses of Betic volcanics and Malaga dykes

Sample:	M11	M9	M2	B322	M5	B302	B319	B312a	B318	B321	B309	B310	B304hb	B304	B305a	B306	B307
Locality:	Malaga	Malaga	Malaga	Malaga	Malaga	Mazarrón	C. de Gata	C. de Gata	C. de Gata	C. de Gata	C. de Gata	C. de Gata	Tallante	Tallante	Jumilla	Cancarix	Vera
Latitude	36°47'	36°46'	36°49'	36°51'	36°50'	37°36'	36°47'	36°55'	36°48'	36°58'	37°14'	37°03'	37°40'	37°40'	38°27'	38°25'	37°13'
Longitude	4°26'	4°26'	4°26'	4°27'	4°27'	1°21'	2°06'	2°03'	2°05'	2°10'	1°50'	1°53'	1°09'	1°09'	1°27'	1°35'	1°56'
SiO ₂ (wt %)	51.57	52.72	53.24	53.81	54.60	52.02	56.37	57.78	59.03	62.66	66.97	69.81	46.04	49.75	50.54	56.33	52.22
TiO ₂	0.78	0.66	0.83	0.75	0.81	1.75	0.64	0.67	0.63	0.59	0.59	0.40	1.59	2.16	1.34	1.58	1.27
Al ₂ O ₃	16.38	15.14	15.74	17.29	16.36	12.80	17.88	16.60	16.97	17.38	15.55	12.99	6.80	17.69	8.90	9.24	10.45
Fe ₂ O ₃	8.35	7.82	9.62	7.76	9.07	14.50	8.40	7.16	6.51	5.22	3.55	2.70	10.80	9.43	6.43	5.27	4.83
MnO	0.13	0.11	0.18	0.13	0.15	0.14	0.14	0.12	0.10	0.07	0.03	0.08	0.15	0.17	0.09	0.08	0.07
MgO	7.42	4.92	5.13	6.32	5.66	4.56	4.00	4.33	3.53	1.82	1.56	1.59	16.79	3.96	15.37	10.79	7.06
CaO	11.01	8.66	9.45	11.01	9.25	8.38	8.61	8.18	6.97	2.50	2.19	2.13	10.41	7.49	4.68	3.44	6.06
Na ₂ O	2.53	2.68	2.43	2.95	2.83	3.72	2.36	2.49	2.85	2.11	2.19	2.13	1.01	5.28	0.81	1.00	3.35
K ₂ O	0.41	0.87	0.30	0.60	0.21	0.78	0.94	1.39	1.55	3.44	4.64	1.13	0.28	1.56	6.80	8.68	2.88
P ₂ O ₅	0.08	0.07	0.08	0.08	0.08	0.24	0.15	0.15	0.16	0.19	0.33	0.08	0.22	0.88	1.63	1.15	0.69
LOI	0.84	6.53	3.05	1.63	0.96	1.00	0.30	1.26	1.48	3.55	1.57	1.41	0.49	2.48	2.48	0.97	9.79
Total	99.50	100.18	100.05	100.51	99.88	99.89	99.79	100.13	100.11	99.64	99.90	99.42	99.58	99.83	99.07	98.53	99.60
Sc (ppm)	40	38	41	43	37	43	27	30	22	13	16	23	40	15	11	14	14
V	204	210	228	218	220	370	191	190	155	110	74	149	186	74	91	74	76
Cr	224	22	6	14	15	14	13	55	16	92	79	137	1100	45	621	286	456
Co	33	28	28	38	20	38	18	20	15	12	10	10	64	26	43	31	26
Ni	62	25	14	45	20	41	5	18	5	23	24	13	320	52	689	544	378
Cu	102	6	50	95	35	93	23	35	14	35	6	18	34	26	47	26	24
Zn	56	39	83	49	46	58	56	54	54	53	53	24	63	97	70	71	61
Ga	14	14	15	15	16	19	17	16	20	22	18	13	11	23	17	19	18
Rb	17.2	42.6	14.4	26.0	8.1	28.3	37.1	62.5	162.4	164.1	190.6	38.5	5.6	32.1	343.8	510.1	384.7
Sr	155	162	170	170	175	305	305	246	254	357	894	146	227	1009	1086	833	451
Y	18.1	20.5	19.3	18.2	20.5	36.4	15.7	20.6	17.3	28.1	26.6	18.2	17.7	28.6	34.4	29.9	22.5
Zr	24.4	36.7	37.5	32.1	49.7	15.5	64.0	87.7	82.7	56.8	109.0	58.1	75.4	319.3	710.4	884.4	670.5
Nb	2.15	2.18	1.86	2.45	2.48	10.02	3.70	4.82	5.25	18.29	19.11	2.88	11.75	102.02	52.24	51.72	39.60
Cs	0.89	1.30	1.25	3.17	0.40	4.75	2.15	3.72	18.79	13.06	20.52	3.07	0.26	6.03	6.10	23.39	87.86
Ba	45	101	50	91	45	1172	237	169	264	722	1324	389	161	1178	3120	2570	1434
La	9.06	3.69	2.89	3.78	5.04	17.77	10.06	14.04	18.50	68.27	51.54	11.21	14.25	74.92	1100.36	111.38	94.79
Ce	9.06	9.16	7.63	9.29	12.09	38.98	21.15	29.23	37.06	131.82	102.43	20.23	30.95	135.05	254.17	292.35	243.09
Pr	1.36	1.40	1.23	1.43	1.75	5.22	2.78	3.70	4.51	15.08	12.93	2.56	4.50	15.31	37.38	43.69	34.88
Nd	6.80	7.25	6.54	7.28	8.52	23.60	11.93	15.76	18.06	56.75	52.75	10.44	21.89	59.00	168.42	199.00	154.06
Sm	1.98	2.21	2.11	2.11	2.45	5.81	2.75	3.49	3.82	10.14	10.44	2.34	5.02	9.62	30.92	34.98	26.68
Eu	0.77	0.74	0.78	0.78	0.85	1.76	0.81	0.88	0.96	2.07	2.09	0.64	5.00	2.82	5.19	5.43	4.13
Gd	2.59	3.02	2.75	2.70	3.02	6.70	2.82	3.67	3.58	8.35	7.82	2.63	5.00	8.11	17.58	17.39	13.78
Tb	0.46	0.51	0.49	0.47	0.54	1.06	0.44	0.58	0.53	1.10	1.03	0.41	0.87	1.08	1.80	1.70	1.33
Dy	2.87	3.22	3.13	2.97	3.31	6.33	2.62	3.35	2.84	5.37	5.12	2.48	3.57	5.53	7.41	6.63	5.17
Ho	0.64	0.72	0.70	0.65	0.73	1.33	0.56	0.70	0.61	0.97	0.92	0.56	1.04	1.20	1.03	1.03	0.80
Er	1.69	1.89	1.86	1.69	1.95	3.32	1.43	1.81	1.58	2.31	2.21	1.52	1.39	2.39	2.59	2.31	1.77
Tm	0.29	0.33	0.32	0.30	0.33	0.54	0.25	0.31	0.26	0.38	0.36	0.26	0.21	0.39	0.40	0.35	0.27
Yb	1.71	1.92	1.71	1.76	2.00	3.02	1.47	1.90	1.64	2.20	2.06	1.58	1.10	2.24	2.35	2.13	1.58
Lu	0.27	0.31	0.30	0.27	0.30	0.44	0.23	0.30	0.26	0.33	0.30	0.26	0.15	0.34	0.34	0.31	0.23
Hf	0.85	1.22	1.16	1.02	1.48	0.78	1.85	2.42	2.62	1.94	3.54	1.69	2.32	7.05	19.59	24.15	18.77
Ta	0.19	0.19	0.18	0.20	0.20	0.62	0.35	0.37	0.50	1.48	1.73	0.31	0.85	1.16	3.17	3.26	2.73
Pb	3.14	4.71	6.83	4.37	1.83	7.48	11.08	12.25	29.51	55.17	88.34	8.76	3.79	14.46	237.72	95.91	57.72
Th	0.75	0.80	0.71	1.23	0.83	3.00	3.00	4.56	8.15	30.76	40.32	3.54	5.88	28.69	115.01	125.95	85.50
U	0.29	0.37	0.34	0.19	0.59	0.43	1.37	1.63	3.58	7.92	12.72	1.93	1.19	6.12	26.10	13.88	19.50
⁸⁷ Sr/ ⁸⁶ Sr	0.70467	0.70783	0.70795	0.70553	0.70621	0.70874	0.71002	0.70996	0.71327	0.71385	0.71144	0.71055	0.70560	0.70454	0.71670	0.71722	0.72073
¹⁵² Nd/ ¹⁴⁴ Nd	0.51281	0.51283	0.51288	0.51285	0.51280	0.51238	0.51235	0.51223	0.51209	0.51209	0.51204	0.51242	0.51258	0.51259	0.51204	0.51199	0.51214
²⁰⁶ Pb/ ²⁰⁴ Pb	18.629	18.693	18.573	18.708	18.573	18.750	18.836	18.810	18.747	18.716	18.820	18.717	18.713	18.828	18.760	18.730	18.808
²⁰⁷ Pb/ ²⁰⁴ Pb	15.627	15.681	15.615	15.682	15.599	15.641	15.670	15.589	15.642	15.653	15.637	15.632	15.562	15.652	15.665	15.629	15.689
²⁰⁸ Pb/ ²⁰⁴ Pb	38.795	38.978	38.813	38.832	38.708	38.822	38.831	38.583	38.861	38.883	38.845	38.796	38.637	38.421	38.931	38.833	39.022

LOI, loss on ignition.

Table 3: Tallante spinel lherzolite xenoliths

Sample:	S1	S3	S4
Latitude (°N):	37°40'	37°40'	37°40'
Longitude (°W):	1°09'	1°09'	1°09'
SiO ₂ (wt %)	44.27	44.39	43.93
TiO ₂	0.06	0.08	0.06
Al ₂ O ₃	2.20	2.41	2.05
Fe ₂ O ₃	8.91	9.43	9.01
MnO	0.13	0.14	0.13
MgO	42.58	42.20	43.26
CaO	2.02	1.91	1.95
Na ₂ O	0.09	0.07	0.08
K ₂ O	0.01	0.01	0.01
P ₂ O ₅	0.02	0.02	0.02
LOI	-0.19	-0.30	-0.25
Total	100.10	100.36	100.25
Sc (ppm)	6	2	4
V	47	44	44
Cr	2094	1775	1698
Co	112	102	106
Ni	2162	1951	2092
Cu	7.62	4.76	7.17
Zn	38.66	36.53	32.86
Ga	1.43	1.65	1.28
Rb	0.52	0.41	0.24
Sr	7.28	3.54	4.33
Y	1.75	1.89	1.78
Zr	2.82	3.65	1.45
Nb	0.51	0.47	0.22
Cs	0.02	0.03	0.01
Ba	2.78	0.25	0.08
La	0.34	0.33	0.29
Ce	0.66	0.68	0.43
Pr	0.10	0.10	0.08
Nd	0.47	0.51	0.43
Sm	0.14	0.16	0.14
Eu	0.05	0.06	0.05
Gd	0.19	0.24	0.22
Tb	0.04	0.04	0.04
Dy	0.27	0.29	0.26
Ho	0.06	0.07	0.06
Er	0.17	0.20	0.18
Tm	0.03	0.04	0.03
Yb	0.19	0.22	0.21
Lu	0.03	0.04	0.04
Hf	0.02	0.05	-0.01
Ta	0.05	0.02	0.02
Pb	0.02	0.01	0.04
Th	0.11	0.12	0.14
U	0.04	0.03	0.04

Ni and Sc, are rather low, consistent with their generally evolved nature.

The calc-alkaline volcanic rocks from the Cabo de Gata and Mazarrón–Cartagena regions form a broadly contiguous array in most major and trace element variation diagrams, extending from compositions similar to the more evolved Malaga dykes up to highly evolved rocks with SiO₂ contents >70% (Fig. 4). This is accompanied by systematic, broadly linear decreases in MgO, Al₂O₃, Fe₂O₃, TiO₂, CaO and Na₂O and increases in K₂O. On the K₂O–SiO₂ diagram (Fig. 4d), these rocks largely fall within the calc-alkaline to high-K calc-alkaline field. Compatible element concentrations are low to very low in all of these rocks. The cordierite–garnet dacites, taken as representative of local crustal melts, fall in the midst of the calc-alkaline volcanic array, having ~63% SiO₂ and 3.5% K₂O.

The Tallante alkali basalts are relatively evolved products with MgO ~4–5%, *mg*-number = 45–50 and low Cr and Ni contents. They have rather low SiO₂ and moderate K₂O (Fig. 4). The hornblende–clinopyroxene cumulate has a complementary composition, with high MgO, Cr and Ni accompanied by low Al₂O₃ and K₂O. The spinel lherzolite xenolith compositions are dominated by their high modal olivine content (~80%, Ancochea & Nixon, 1987) and have high MgO and *mg*-number = 90, and low TiO₂ and CaO (Table 3).

Finally, the lamproites have high MgO, Ni and Cr with *mg*-numbers of 74–83, suggesting that they crystallized from primary mantle melts. They have relatively high SiO₂ but distinctly low Al₂O₃, Fe₂O₃ (total iron) and Na₂O for a given MgO or SiO₂ (Tables 2 and A1, Fig. 4). K₂O contents are high, and place the lamproites in the shoshonitic field in Fig. 3d. Thus, they are distinct from the other Neogene magmatic rocks in the Betics (Fig. 3), having extreme compositions, even for lamproites (e.g. Venturelli *et al.*, 1984).

Incompatible trace elements

The general incompatible trace element characteristics are illustrated in primitive mantle normalized multi-element diagrams in Fig. 5 and in chondrite-normalized REE diagrams in Fig. 6. The Malaga dykes have low concentrations of most moderately incompatible trace elements and relatively flat REE patterns (Fig. 6a), similar to those of mid-ocean ridge basalts (MORB). However, they differ significantly from MORB in their enrichment of Rb, U, K, Pb and the light REE (LREE), and by having small negative Ti, Ta–Nb and Zr–Hf anomalies (Fig. 5a). Th and U show some scatter. They are characterized by sub-chondritic Nb/Ta ratios of 11–14, and one sample (M9) shows a small negative Eu anomaly (Fig. 6a).

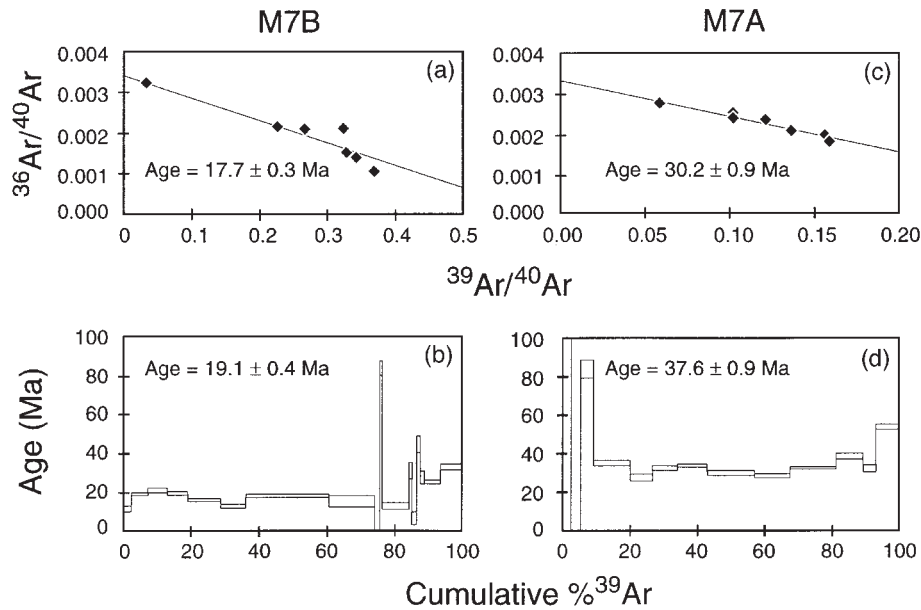


Fig. 3. Plateau and isochron data for basic dyke whole rocks from the Malaga area, M7B-4 (left) and M7A-7 (right). Isochron data (above the respective release data) were used to calculate ages taking into account variations in the sub-plateaux.

The calc-alkaline volcanic rocks generally show a much greater degree of enrichment of the more incompatible trace elements, such as Rb, Th and U, and are markedly LREE enriched (Figs 5b and 6b). They have prominent negative Ba, Ta–Nb and Ti anomalies and a large positive Pb anomaly (Fig. 5b). In detail, the Cabo de Gata REE patterns are generally parallel to each other and strongly LREE enriched. However, they show relatively flat patterns from Dy to Lu and show variable development of a negative Eu anomaly (Fig. 6b). The REE pattern for sample B302 from Mazarrón is enriched in HREE relative to the Cabo de Gata volcanic rocks, whereas sample B309 shows a pattern more like the cordierite–garnet dacite (B321) than the other calc-alkaline volcanic rocks. Like the Malaga dykes, these rocks are also characterized by sub-chondritic Nb/Ta ratios of 9–13, excepting B302 (Nb/Ta = 16). The cordierite–garnet dacite has an incompatible trace element pattern which is broadly parallel with the calc-alkaline rocks in Fig. 5b but with higher overall concentrations; exceptions are formed by negative anomalies for Sr, P and Zr–Hf (see Fig. 5b). Its REE pattern is significantly more LREE enriched than the calc-alkaline volcanic rocks (excepting B309) but with similar heavy REE (HREE) concentrations (Fig. 6b).

In contrast to the other three suites of rocks, the Tallante alkali basalts have reasonably smooth, convex-up incompatible trace element patterns, typical of alkali basalts (Fig. 5c). Departures from the smooth patterns

involve a negative K anomaly and a positive anomaly at Pb. The REE patterns are LREE enriched with relatively flat HREE and no Eu anomaly (Fig. 6c). The hornblende–clinopyroxene cumulate has an incompatible element pattern which broadly mirrors that of its host lava, albeit at lower concentrations. Its REE pattern is also similar to that of the host lava but has higher middle REE (MREE) concentrations. The spinel lherzolite xenoliths have very low incompatible trace element concentrations and relatively flat patterns except for negative anomalies at Ba and K (Fig. 5c). Their REE patterns are essentially flat with rather high concentrations (1–2 times chondrite) and, again, no Eu anomaly.

The overall patterns of the lamproites are broadly similar to those of the calc-alkaline rocks in terms of having negative Ba, Ta–Nb and Ti anomalies. However, they are distinguished by far more extreme enrichment of the more incompatible elements and a strikingly large positive Pb anomaly (Fig. 5d). Additionally, the lamproites possess negative Sr and P anomalies, and K is significantly depleted relative to Th and U despite the high overall K abundances. The REE patterns for the lamproites are distinct from those of all the other Neogene Betic volcanic rocks, and the LREE abundances reach up to 400–500 times chondrite. These patterns are strongly sigmoidal, with flat LREE and HREE, steep MREE, and have negative Eu anomalies (Fig. 6d).

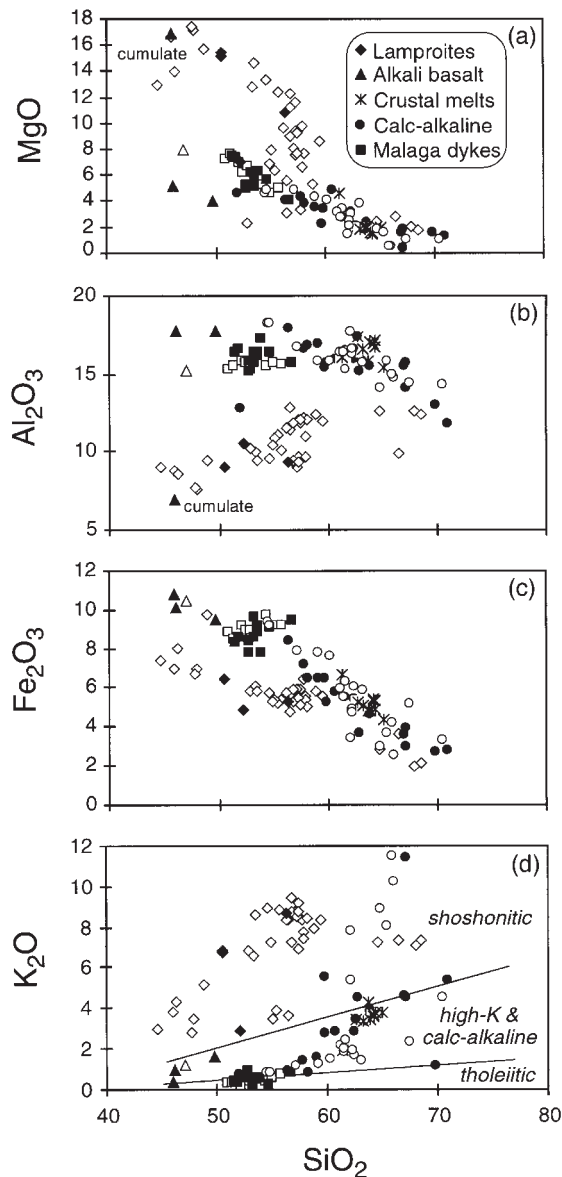


Fig. 4. Major element variation diagrams highlighting the distinction between the lamproites and the Malaga dykes and calc-alkaline volcanic rocks which form a broadly contiguous array (see text for discussion). The data from this study (shown as filled symbols) are supplemented with published data (shown as open symbols) from the following sources: Malaga dykes (Torres-Roldán *et al.*, 1986); calc-alkaline volcanics (Di Battistini *et al.*, 1987); cordierite dacites (Munksgaard, 1984) taken as representative of crustal melts; Tallante alkali basalts (Ancochea & Nixon, 1987); lamproites (Nixon *et al.*, 1984; Venturelli *et al.*, 1984; Nelson *et al.*, 1986).

Radiogenic isotopes

The four rock suites are well distinguished by their $^{143}\text{Nd}/^{144}\text{Nd}_i$ – $^{87}\text{Sr}/^{86}\text{Sr}_i$ systematics (Fig. 7a). The Malaga dykes have relatively restricted $^{143}\text{Nd}/^{144}\text{Nd}_i$ (0.5129–0.5128); however, their $^{87}\text{Sr}/^{86}\text{Sr}_i$ ratios range from 0.705 to 0.709

and the highest $^{87}\text{Sr}/^{86}\text{Sr}_i$ ratios may reflect alteration, as these occur in samples M9 and M2, which also have elevated loss on ignition (Table 1). In contrast, the calc-alkaline rocks are displaced to much lower $^{143}\text{Nd}/^{144}\text{Nd}_i$ and higher $^{87}\text{Sr}/^{86}\text{Sr}_i$. The cordierite–garnet dacite, taken as representative of local crustal rocks, has the highest $^{87}\text{Sr}/^{86}\text{Sr}_i$ ratio. The Tallante alkali basalt and cumulate have $^{143}\text{Nd}/^{144}\text{Nd}_i \sim 0.5126$ and $^{87}\text{Sr}/^{86}\text{Sr}_i = 0.705$ – 0.706 . The lamproites have extreme isotope ratios with significantly lower $^{143}\text{Nd}/^{144}\text{Nd}_i$ and higher $^{87}\text{Sr}/^{86}\text{Sr}_i$ than either the crustal melt or the calc-alkaline rocks (e.g. Nelson *et al.*, 1986).

The Betic dykes and volcanic rocks have elevated $^{207}\text{Pb}/^{204}\text{Pb}$ and $^{208}\text{Pb}/^{204}\text{Pb}$ at a given $^{206}\text{Pb}/^{204}\text{Pb}$ ratio, and all lie well above the northern hemisphere reference line (NHRL) of Hart (1984), with the exception of the Tallante lava, which lies close to the NHRL. In the $^{207}\text{Pb}/^{204}\text{Pb}$ – $^{206}\text{Pb}/^{204}\text{Pb}$ diagram (Fig. 7b), the Malaga dykes form a linear array roughly parallel to, and above, the NHRL. The lamproites crudely form an extension of this array to higher $^{206}\text{Pb}/^{204}\text{Pb}$. The calc-alkaline volcanic rocks lie below this array, with lower $^{207}\text{Pb}/^{204}\text{Pb}$ and a range of $^{206}\text{Pb}/^{204}\text{Pb}$ ratios that encompasses the range shown by the lamproites. The cordierite–garnet dacite lies at the low $^{206}\text{Pb}/^{204}\text{Pb}$ end of this array and thus at lower $^{207}\text{Pb}/^{204}\text{Pb}$ than the Malaga dykes and lamproites. Finally, and in contrast to the other rocks, the Tallante lava has much lower $^{207}\text{Pb}/^{204}\text{Pb}$ and lies on the NHRL at the high $^{206}\text{Pb}/^{204}\text{Pb}$ end of the spectrum shown by the Betic rocks. Interestingly, the Tallante cumulate has higher $^{207}\text{Pb}/^{204}\text{Pb}$ and lower $^{206}\text{Pb}/^{204}\text{Pb}$, and lies near the field of the calc-alkaline volcanic rocks. Similar relationships are observed in the $^{208}\text{Pb}/^{204}\text{Pb}$ – $^{206}\text{Pb}/^{204}\text{Pb}$ diagram (Fig. 7c).

PETROGENESIS OF THE BETIC MAGMATIC ROCKS

In the following sections we investigate, in chronological order, the petrogenesis of the four Neogene rock suites in SE Spain, after which we look at how these constraints can be interpreted within the context of orogenic collapse of the Betic Cordillera. As this is our specific objective, and because the number of analyses for each rock suite are limited, the following sections focus on specific aspects such as depth of melt generation, degree of partial melting and the nature of the source region, and are not necessarily intended to represent an exhaustive petrogenetic analysis.

Malaga dykes

The Malaga dykes are mantle-derived tholeiites which record a crystallization history that involved moderate

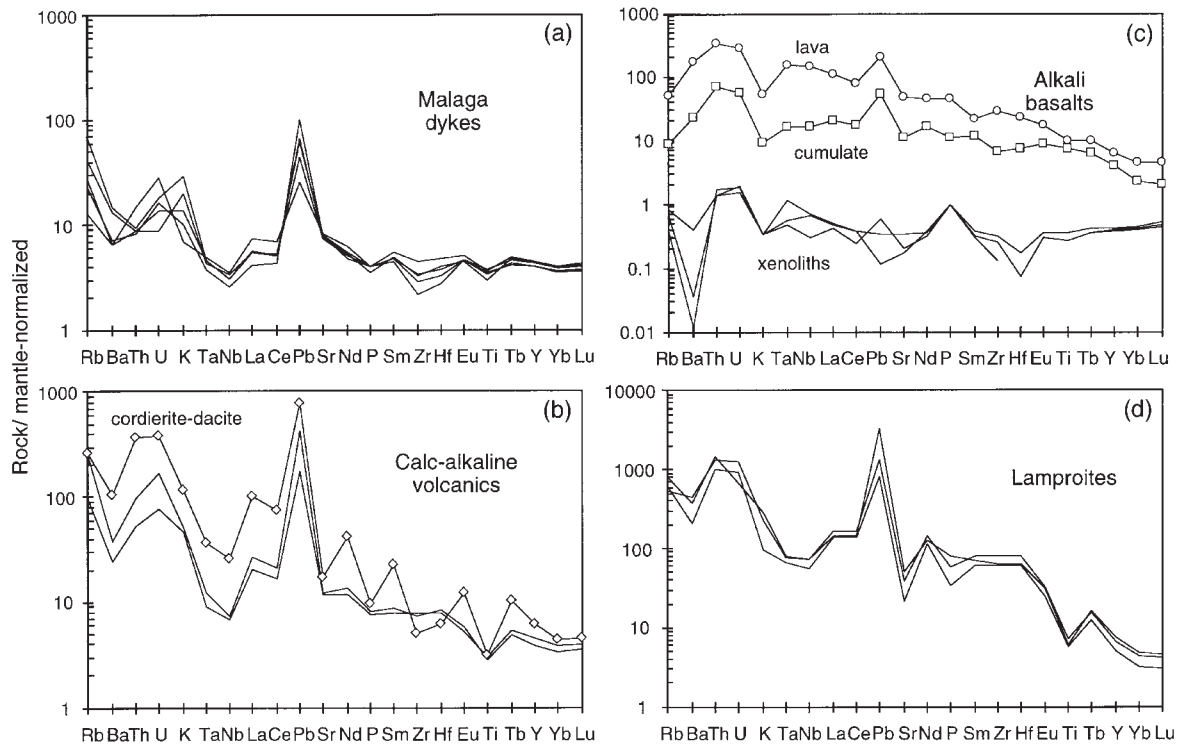


Fig. 5. Incompatible trace element diagrams for the four different rock suites in the Betic-Alboran Domain (see text for discussion). Normalized to primitive mantle values from Sun & McDonough (1989).

Fe enrichment (Torres-Roldán *et al.*, 1986). Although crustal contamination has clearly occurred (see below), the relatively low Fe and high Si in the least contaminated, highest-MgO dykes suggest that partial melting took place at relatively shallow levels (e.g. Klein & Langmuir, 1987). Consistent with this, they also possess relatively flat REE patterns and have HREE concentrations that are 10–15 times chondritic values, indicating that partial melting did not take place in the presence of residual garnet. Figure 8a is a plot of $Tb/Yb-La/Yb$ in which curves for partial melting of a primitive mantle composition within shallow spinel facies and deeper garnet facies peridotite are shown. The Malaga dykes have not undergone significant REE fractionation and lie close to the primitive mantle composition, despite the majority of them being relatively evolved diorites. Figure 8b is a plot of Nb/Zr vs Nb , which should discriminate between the effects of partial melting and fractionation, assuming that both elements are incompatible with respect to the source mineralogy. In this diagram, the Malaga dykes largely fall around a mantle partial melting curve indicating degrees of partial melting generally $>5\%$ and more typically around 10–15%, which is consistent with their tholeiitic character and REE inversion modelling (D. P. McKenzie, personal communication, 1998). Given

these degrees of partial melting, their low Tb/Yb indicates that partial melting took place in the spinel facies (Fig. 8a) and thus at depths shallower than 60–70 km. The sub-chondritic Nb/Ta ratios may indicate that the mantle source had undergone an episode of prior melt depletion (Plank & White, 1995).

The Malaga dykes have small negative Ta–Nb, Ti and Zr–Hf anomalies, and positive Rb, U, K and Pb anomalies (Fig. 5a). Additionally, their $^{87}Sr/^{86}Sr_i$ and $^{143}Nd/^{144}Nd_i$ isotope ratios are higher and lower, respectively, than those of the contemporary depleted mantle ($^{87}Sr/^{86}Sr \sim 0.7029$ and $^{143}Nd/^{144}Nd \sim 0.5132$) and they are displaced well above the NHRL with elevated $^{208}Pb/^{204}Pb$ and $^{207}Pb/^{204}Pb$. Thus, these rocks clearly do not represent unmodified melts from the depleted upper mantle. Elevated $^{87}Sr/^{86}Sr_i$ and negative Ta–Nb anomalies suggest mixing with a contaminant bearing a crustal signature. In a plot of Zr/Nb vs Ti/Nb (Fig. 9a) the Malaga dykes form a scattered array between MORB-like compositions and those of the lamproites and crustal melts. Consistent with the inferences from the isotopic data, this suggests that the dykes could have been affected either by crustal contamination or by mixing with lamproitic partial melts from the lithospheric mantle as the magmas rose towards the surface (e.g. Ellam & Cox,

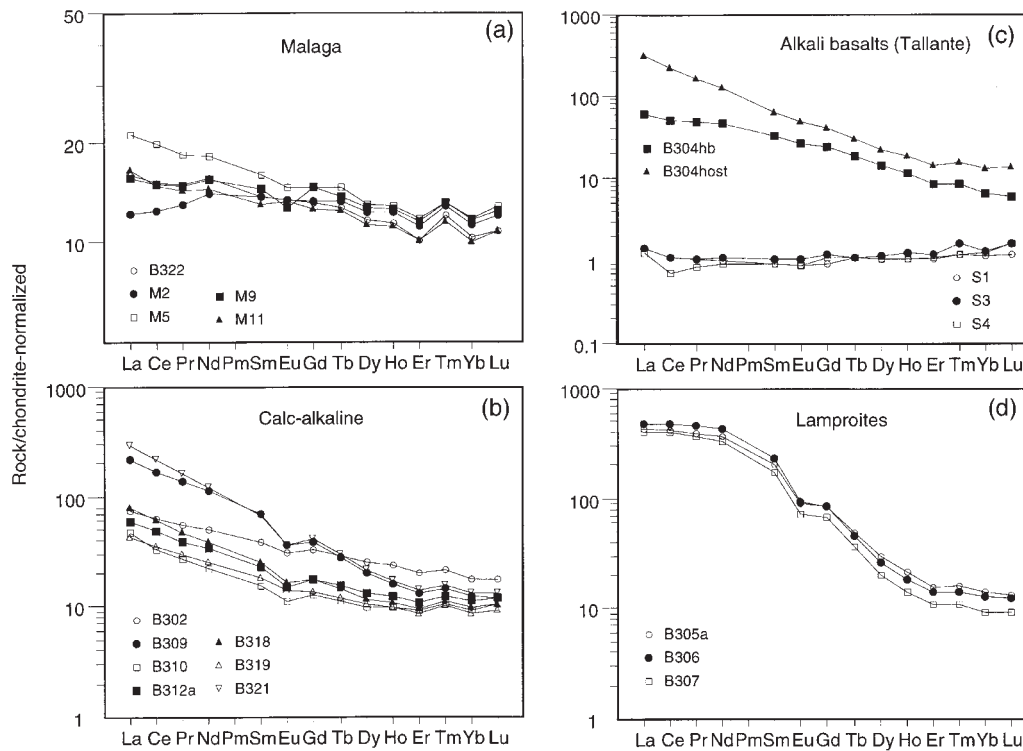


Fig. 6. Chondrite-normalized REE diagrams. The flat patterns for the Malaga dykes and the development of a negative Eu anomaly in the calc-alkaline volcanics should be noted. The lamproites are characterized by sigmoidal patterns with negative Eu anomalies. The Tallante alkali basalt lava is LREE enriched whereas the spinel lherzolite xenoliths have mildly LREE-depleted patterns.

1991). The lamproites are characterized by high K_2O and have low Al_2O_3 compared with the crustal melts (Fig. 4), and so K_2O/Al_2O_3 should readily distinguish between these two possibilities. Figure 9b shows that the Malaga dykes form the low- SiO_2 end of a tight array with the calc-alkaline volcanic rocks which ends in the field of the crustal melts. By contrast, the majority of the lamproites have much higher K_2O/Al_2O_3 and lower SiO_2 . It therefore seems clear that crustal, rather than lithospheric mantle, contamination is responsible for the trend towards elevated $^{87}Sr/^{86}Sr_i$. Although there are insufficient data for a rigorous analysis, Fig. 10 shows that the compositional array of the Malaga dykes can be approximated by calculated MORB–crust mixing curves. Approximately 5–15% crustal contamination is indicated, though, as discussed above, the higher $^{87}Sr/^{86}Sr_i$ in samples M2 and M9 may reflect alteration. It is also likely that crustal contamination was coupled with increasing degrees of fractional crystallization (e.g. DePaolo, 1981), as SiO_2 increases and Eu/Eu^* decreases with increasing $^{87}Sr/^{86}Sr_i$ (Fig. 10a and b). Notwithstanding the limitations of the data, the critical observation from Fig. 10 is that the negative Nb anomalies (as measured by Ce/Nb) and elevated $^{87}Sr/^{86}Sr_i$ ratios of the Malaga dykes can be explained by crustal contamination (Fig. 10c). The data

arrays project back to compositions typical of MORB and there is no requirement for a unique source composition such as subduction-modified mantle wedge or enriched lithospheric mantle.

Cabo de Gata and Mazarrón–Cartagena calc-alkaline volcanic rocks

Although apparently erupted significantly later, the calc-alkaline volcanic rocks appear to form a continuum with the Malaga dyke arrays. They exhibit a large compositional range with MgO , Al_2O_3 and Fe_2O_3 decreasing, and K_2O increasing, as SiO_2 increases (Fig. 4), implying an important role for crystal fractionation in their petrogenesis (e.g. Di Battistini *et al.*, 1987). Compared with the Malaga dykes they are much more enriched in the more incompatible trace elements whereas their REE fractionation is similar, also precluding partial melting in the presence of residual garnet (see Fig. 8a). In Fig. 8b the calc-alkaline volcanic rocks spread out from the theoretical partial melting curve, and the Malaga dyke array, to higher Nb, consistent with increases in Nb content induced by fractionation \pm contamination.

The calc-alkaline volcanic rocks have larger negative Ba, Ta–Nb and Ti anomalies than the Malaga dykes,

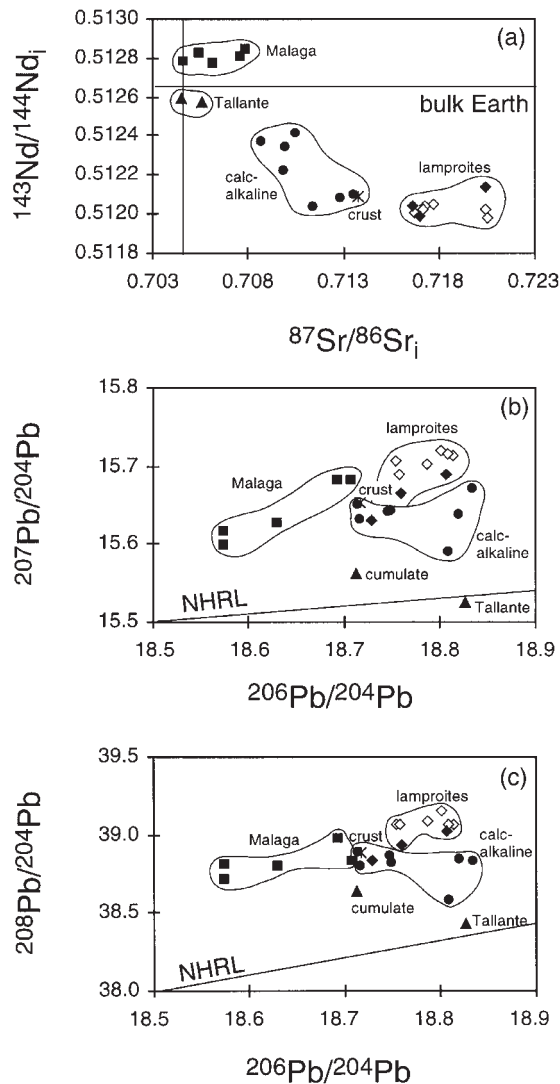


Fig. 7. Nd–Sr and Pb–Pb isotope diagrams (see text for discussion). Symbols and data sources as in Fig. 4; northern hemisphere reference line (NHRL) from Hart (1984).

similar to those exhibited by the cordierite–garnet dacites. These dacites have $\delta^{18}\text{O}$ values ranging from +12.2 to +15.6‰ and formed by partial melting of semi-pelitic source rocks (Munksgaard, 1984). The low Sr and negative Eu, P and Zr–Hf anomalies exhibited by these rocks probably reflect residual plagioclase, clinopyroxene and accessory phases (zircon and apatite) during partial melting. Compared with the Malaga dykes, the calc-alkaline volcanic rocks are displaced to higher $^{87}\text{Sr}/^{86}\text{Sr}_i$ and lower $^{143}\text{Nd}/^{144}\text{Nd}_i$, $^{208}\text{Pb}/^{204}\text{Pb}$ and $^{207}\text{Pb}/^{204}\text{Pb}$. In the $^{87}\text{Sr}/^{86}\text{Sr}_i$ – $^{143}\text{Nd}/^{144}\text{Nd}_i$ diagram (Fig. 7a) they form a broad negative array which extends to much lower $^{87}\text{Sr}/^{86}\text{Sr}_i$ and higher $^{143}\text{Nd}/^{144}\text{Nd}_i$ than the cordierite–garnet dacite crustal melt, suggesting that these rocks do not

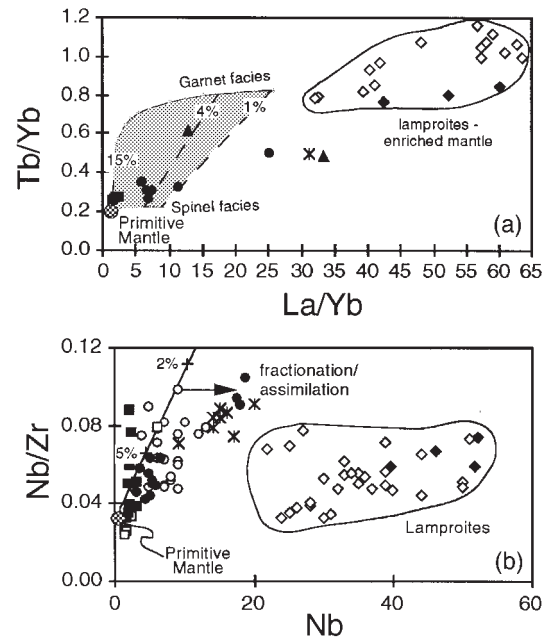


Fig. 8. Partial melting models for the Betic–Alboran Domain rocks. (a) Tb/Yb vs La/Yb diagram with partial melting curves (percent melting indicated) for both spinel and garnet facies upper mantle. The shaded region encompasses the field of likely upper-mantle melts. The Malaga dykes and less crustally contaminated calc-alkaline volcanic rocks lie within this field close to the spinel facies curve, consistent with their derivation by partial melting of the asthenosphere at shallow levels (<70 km). In contrast, the lamproites and alkali basalts have much higher La/Yb, requiring an LREE-enriched mantle source inferred to lie within the sub-continental mantle lithosphere. (b) Nb/Zr vs Nb diagram to separate the effects of partial melting and fractionation–assimilation. The Malaga dykes and calc-alkaline volcanic rocks broadly straddle an asthenospheric partial melting vector (amounts of partial melting indicated) but lie increasingly to the left of this line at higher Nb/Zr, consistent with the combined effects of fractionation and crustal assimilation. As in (a), the lamproites fall well off the melting curve and require an enriched mantle source. Modelling assumed batch partial melting of a MORB mantle peridotite source with distribution coefficients taken from the compilation by Halliday *et al.* (1995). Symbols and data sources as in Fig. 4.

simply reflect crustal melts. None the less, the cordierite–garnet dacite lies at one end of the Sr–Nd (but not Pb–Pb; see discussion below) isotope array formed by the calc-alkaline rocks, and the calc-alkaline volcanic rocks also lie at the end of the Malaga dyke array close to the crustal melts and lamproites in Fig. 9a. The implication is that they represent more contaminated and fractionated equivalents of the Malaga magmas.

In Fig. 10, the calc-alkaline volcanic rocks scatter around the same MORB–crust mixing curves as the Malaga dykes, though the implied amounts of crustal contamination are significantly higher (20–60%). It should be noted that, although the lamproites also lie at the end of these arrays, Fig. 9b rules out the lamproites as an end member for these rocks. Thus, partial melting of the crust has played a major role in the magmatism

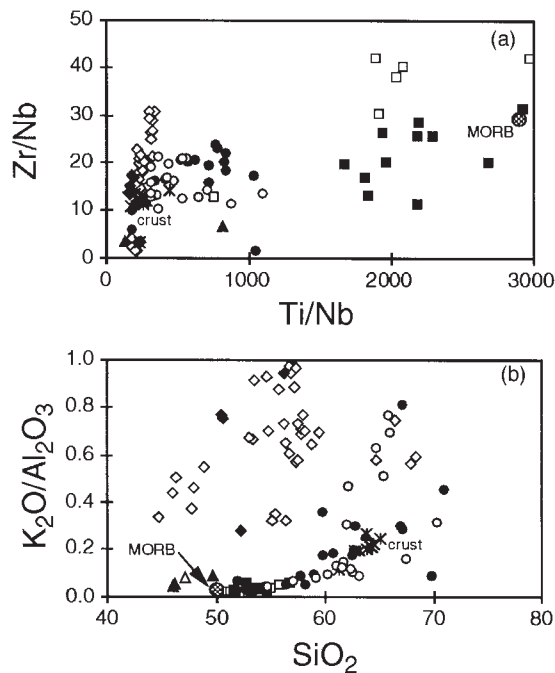


Fig. 9. (a) Zr/Nb vs Ti/Nb diagram showing that the Malaga dykes scatter around a composition broadly similar to MORB whereas the lamproites form a steep positive array. The calc-alkaline volcanic rocks lie between the Malaga dyke suite and the lamproite–crustal melt fields, implying a mixing relationship. (b) K_2O/Al_2O_3 vs SiO_2 to distinguish between a crustal or lamproitic contaminant for the Malaga dyke–calc-alkaline volcanic suites. The Malaga dyke–calc-alkaline volcanic rocks form a tight array extending towards the crustal melts whereas the lamproites have higher K_2O/Al_2O_3 and generally lower SiO_2 . Symbols and data sources as in Fig. 4.

in the Betic–Alboran Domain, and the coupled increases in SiO_2 and $^{87}Sr/^{86}Sr$ combined with decreasing Eu/Eu^* (Fig. 10a and b) provide good evidence that crustal contamination was coupled with crystal fractionation. As discussed above for the Malaga dykes, Fig. 10c suggests that the negative Ta–Nb anomaly in these rocks could be accounted for by crustal contamination of MORB-like magmas. A similar mantle source to that of the Malaga dykes is suggested by the similarly sub-chondritic Nb/Ta ratios of the calc-alkaline rocks. The implied amounts of crustal contamination can explain also the high $^{208}Pb/^{204}Pb$ (Fig. 11) and $^{207}Pb/^{204}Pb$ (not shown) ratios of these rocks. However, the same is not true for the $^{206}Pb/^{204}Pb$ variations, as the cordierite dacite lies between the Malaga dykes and calc-alkaline volcanic rocks in Fig. 7b and c. Unfortunately, with only a single Pb isotope analysis of the local crustal rocks, a more detailed assessment of the significance of this discrepancy must await more detailed work. The large positive Pb spike, which characterizes all of the rocks in Fig. 5, suggests that some process is dominating the Pb budget and by inference also controlling the Pb isotope signature.

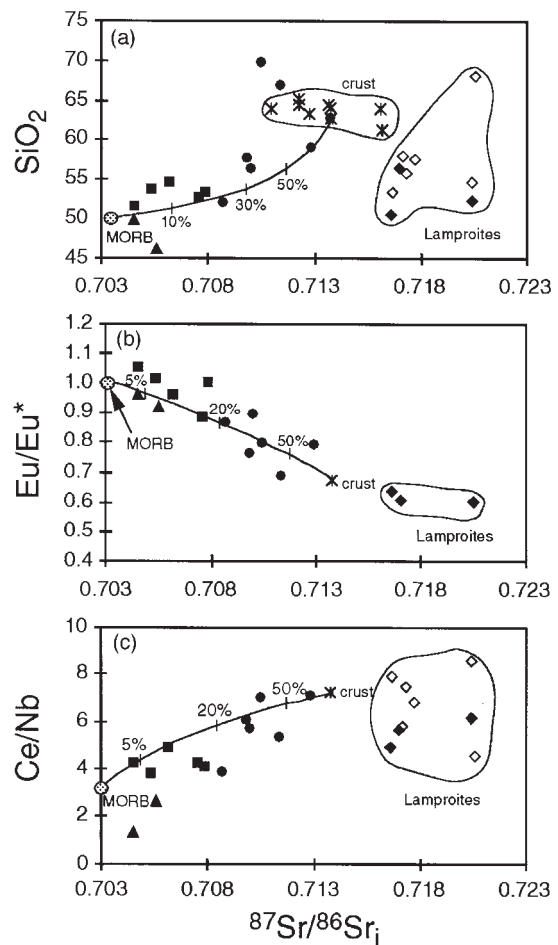


Fig. 10. MORB–crust mixing curves compared with the Malaga dyke–calc-alkaline volcanic array in diagrams of (a) SiO_2 , (b) Eu/Eu^* and (c) Ce/Nb vs $^{87}Sr/^{86}Sr_i$, suggesting the Malaga dykes have been contaminated by 5–20% of a crustal component whereas the crustal contribution to the calc-alkaline volcanic rocks ranges from 20 to 100%. It should be noted that the elevated $^{87}Sr/^{86}Sr_i$ for two of the Malaga dykes may in part reflect alteration; our choice of $^{87}Sr/^{86}Sr_i$ for these diagrams was motivated by the availability of additional literature data for the lamproites and crustal melts. Symbols and data sources as in Fig. 4.

Tallante alkali basalt and xenoliths

Some time after emplacement of the Malaga dykes and the onset of calc-alkaline volcanic activity, alkali basalts were erupted around Tallante. The presence of the cumulate nodules in these lavas provides evidence for clinopyroxene–hornblende fractionation, and the relatively smooth incompatible trace element patterns of the Tallante alkali basalts and their lack of depletion in Ba or Ta–Nb relative to Th and La indicate that they have not significantly interacted with the continental crust. Thus, although data on the alkali basalts remain scarce, these lavas and their inclusions may provide important insights into processes occurring in the mantle beneath the Betic Cordillera.

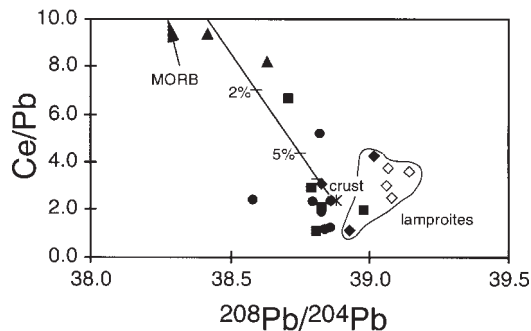


Fig. 11. Ce/Pb vs $^{208}\text{Pb}/^{204}\text{Pb}$, illustrating that contamination of asthenospheric magmas by as little as 5% of a crustal component dominates the Pb isotope budget of the resultant lavas. Symbols and data sources as in Fig. 4.

Partial melting models show that the observed LREE concentrations (200 times chondrite) and La/Yb ratios of 33, exhibited by the Tallante lava, cannot be produced from a primitive mantle source, even by very small degrees (<1%) of melting (Fig. 8a). The high La/Yb relative to Tb/Yb for this lava suggests an origin involving partial melting of an LREE-enriched mantle source. The elevated HREE concentrations and flat HREE patterns suggest that garnet was not a major residual phase, which would be consistent with the presence of spinel lherzolite (and absence of garnet lherzolite) xenoliths and implies a relatively shallow mantle source region. The absence of residual garnet, the need for an LREE-enriched source, and the elevated $^{87}\text{Sr}/^{86}\text{Sr}_i$ and low $^{143}\text{Nd}/^{144}\text{Nd}_i$ isotope ratios of the lava (Fig. 7a), rule out the asthenosphere as the source of these lavas. Moreover, the lack of negative Ta–Nb or Ti anomalies (Fig. 5c), which characterize the local crust, indicates that the elevated $^{87}\text{Sr}/^{86}\text{Sr}_i$ and low $^{143}\text{Nd}/^{144}\text{Nd}_i$ isotope ratios of the Tallante alkali basalts are unlikely to have resulted from crustal contamination.

Although the incompatible trace element patterns for the Tallante alkali basalts (and cumulate) are relatively smooth, they are both characterized by negative K anomalies and positive Pb anomalies, which are likely to reflect real source features. Venturelli *et al.* (1984) noted that phlogopite in these lavas has a higher Ni/MgO ratio than coexisting olivine, an observation they attributed to disequilibrium partial melting of a phlogopite-bearing source. The notion of a relatively shallow, enriched mantle source region for the Tallante alkali basalts is also supported by the observation of veining and metasomatism in some of the spinel lherzolite xenoliths and their relatively low equilibration temperatures of $\sim 850^\circ\text{C}$ (Ancochea & Nixon, 1987), which would correspond to depths of ~ 70 km for a typical continental geotherm and are consistent with the absence of a garnet signature. The Cr, Ni, CaO, Al_2O_3 and MgO contents of the three xenoliths analysed here (Table 3) are typical of mantle

residues (rather than cumulates). However, these xenoliths have relatively flat REE patterns (Fig. 6c) and incompatible trace element concentrations are atypical of those expected in a mantle residue. Indeed, their negative Ba and K anomalies may reflect enrichment by partial melts that were themselves in equilibrium with residual amphibole or phlogopite. This sort of enrichment, either by fluids or small degree partial melts from the convecting upper mantle, may be characteristic of the lower mechanical boundary layer of the lithosphere, i.e. that part of the lower lithospheric mantle which does not convect and so can preserve trace element anomalies and develop resultant isotope anomalies over geological time-scales (e.g. McKenzie, 1989). If so, the Nd-depleted mantle model age for the Tallante alkali basalts suggests this occurred around 700 Ma. However, this constraint is significantly relaxed if enrichment occurred by addition of small partial melts from a mantle plume, in which case the age of enrichment could be significantly younger than 700 Ma.

Lamproites

The origins of the Spanish lamproites have been discussed in some detail previously (Nixon *et al.*, 1984; Venturelli *et al.*, 1984, 1988; Nelson *et al.*, 1986). The *mg*-numbers of the lamproites (74–83) and their olivine phenocrysts (Fo_{90-94} , Venturelli *et al.*, 1984, 1988) suggest that these rocks represent relatively unmodified primary mantle melts. Nevertheless, they are also characterized by having high SiO_2 but distinctly low Al_2O_3 , Fe_2O_3 (total iron) and Na_2O relative to melts known to have come directly from the depleted upper mantle. Such features suggest derivation from peridotite that had been depleted during a previous melt extraction event (e.g. Turner & Hawkesworth, 1995). Similarly, Venturelli *et al.* (1984) observed that the high Ni/MgO ratios of both the whole rocks and their phlogopite phenocrysts probably requires their source was melt depleted. As melt depletion can result in a mantle source with sub-chondritic Nb/Ta it is interesting that the lamproites have chondritic Nb/Ta ratios of 16–18; however, this ratio may have been increased by subsequent source enrichment events (see below) and/or by small degrees of partial melting.

Another striking feature of the lamproites is their extreme degree of enrichment in incompatible trace elements. The concentrations of these elements are significantly higher than in the local crustal melts, which in conjunction with the primary nature of these rocks makes models in which their trace element or isotope signatures reflect solely the effects of crustal contamination untenable. Moreover, Fig. 8a and b shows that the LREE–HREE fractionation and incompatible trace element concentrations in these rocks cannot be produced from

a primitive mantle source even by unrealistically low degrees (<1%) of partial melting (e.g. Venturelli *et al.*, 1984). This difficulty is further compounded by the major element evidence for prior melt depletion of the source, which would have effectively stripped it of all its incompatible elements. Thus, the data require at least a two-stage source history in which addition of incompatible trace elements occurred in an enrichment event subsequent to melt depletion and the high K_2O/Na_2O ratios and the sigmoidal REE patterns may require an even more complex, two- or three-stage, source history (e.g. Venturelli *et al.*, 1984). Such mantle source histories of melt extraction followed by enrichment events are a characteristic of old continental mantle lithosphere (e.g. Hawkesworth *et al.*, 1990; Turner & Hawkesworth, 1995).

In more detail, the relatively high concentrations and flat pattern of the HREE suggests that these melts did not form in the presence of residual garnet, although their source region was probably enriched by a component that had seen residual garnet (e.g. Nixon *et al.*, 1984). Additionally, some of the lamproites host spinel lherzolite xenoliths bearing evidence for veining and metasomatism (Ancochea & Nixon, 1987). Both pieces of evidence are consistent with a relatively shallow, lithospheric origin for these rocks. Phlogopite is a liquidus phase in these rocks and the high K_2O contents of the lamproites mean that these melts would have been increasingly saturated in phlogopite at higher pressures, though the presence of phlogopite and absence of garnet constrain the depth of the source region to <2.5 GPa (Edgar *et al.*, 1976; Mengel & Green, 1989). Thus, given the primary nature of the lamproites, we suggest that their source region contained phlogopite (and probably also apatite; Venturelli *et al.*, 1988). Furthermore, the low concentrations of K relative to Th or La in Fig. 5d, and evidence that K has been buffered relative to other incompatible trace element ratios or concentrations (Fig. 12a and b), indicate that phlogopite was a residual phase during partial melting. Venturelli *et al.* (1988) have suggested that partial melting may have occurred at relatively shallow pressures at a phlogopite + olivine + orthopyroxene + liquid peritectic. Even more intriguingly, Nb shows an almost identical behaviour to K, with Nb/Zr decreasing as Ce/Y increases (Fig. 12c) and Nb concentrations showing little or no correlated increase with increasing Zr, even though Nb concentrations span a considerable range (Fig. 12d). Thus, it would appear that Nb concentrations have also been controlled by a residual source phase. The most obvious candidates would be a residual Ti-rich phase such as rutile or ilmenite, which might be stabilized at elevated oxygen fugacities within the lithospheric mantle. However, Fig. 13 shows that Nb concentrations increase as the size of the negative Ti anomaly in Fig. 5d increases. Therefore this phase is unlikely to be a residual Ti-rich phase. The similarity in the behaviour of

K and Nb (Fig. 12) suggests that the same phase may be responsible for the buffering of concentrations of both elements, and recent data from subduction metasomatized mantle xenoliths show that phlogopite can contain appreciable concentrations of Nb and Ta (Ionov & Hofmann, 1995).

The enrichment event(s) that affected the lithospheric mantle source region of the lamproites resulted in the addition of incompatible elements, including volatiles conducive to phlogopite stabilization. If this enrichment resulted from the addition of small partial melts from the depleted upper mantle (e.g. McKenzie, 1989), then the elevated $^{87}Sr/^{86}Sr_i$ and low $^{143}Nd/^{144}Nd_i$ of the lamproites would suggest that this occurred in the Proterozoic, as the Nd-depleted mantle model ages for the lamproites are 1.6–1.9 Ga. However, the Spanish lithosphere may not be old enough for this isotope ingrowth model (Nelson *et al.*, 1986), and such a model does not easily explain the negative Eu anomalies that characterize these rocks. Such features are unlikely to have developed during partial melting. Negative Eu anomalies can be produced by plagioclase, as either a residual or a fractionating phase. However, plagioclase is not generally stable at mantle depths and is not a liquidus phase in the lamproites, which approximate primary melts and thus cannot have undergone significant crystal fractionation. The alternative is that the enrichment process involved the addition of ancient incompatible element enriched material, which itself already possessed these trace element and isotopic characteristics. Nelson *et al.* (1986) have noted that the elevated $^{208}Pb/^{204}Pb$ and $^{207}Pb/^{204}Pb$ of the lamproites is most similar to modern oceanic pelagic sediments and would be consistent also with their high $^{87}Sr/^{86}Sr_i$ and low $^{143}Nd/^{144}Nd_i$. Furthermore, negative Ta–Nb, Ti and Eu anomalies are features of crustal sediments and therefore it is argued that the mantle source region of the lamproites was enriched by the addition of small amounts (~2–3% on the basis of the Ce/Pb and Eu/Eu* ratios) of a sediment component, most probably partial melts of sediments introduced during an ancient subduction event (e.g. Hergt *et al.*, 1989).

Direct evidence for fluxing of the mantle beneath the Betic–Alboran Domain with fluids containing crustal components comes from the geochemistry of the peridotites and pyroxenites of the Ronda (Reisberg & Zindler, 1986) and Beni Bousera peridotites (Pearson *et al.*, 1991, 1993; Kumar *et al.*, 1996). The pyroxenites at Beni Bousera have anomalously high oxygen isotope compositions (Pearson *et al.*, 1991), which, together with their radiogenic isotope systematics that overlap those of the lamproites and Tallante alkali basalt, indicate a sediment-derived component in their source (Pearson *et al.*, 1993). Model Nd and Os ages are Proterozoic (Pearson *et al.*, 1993; Kumar *et al.*, 1996) and hence may support ancient

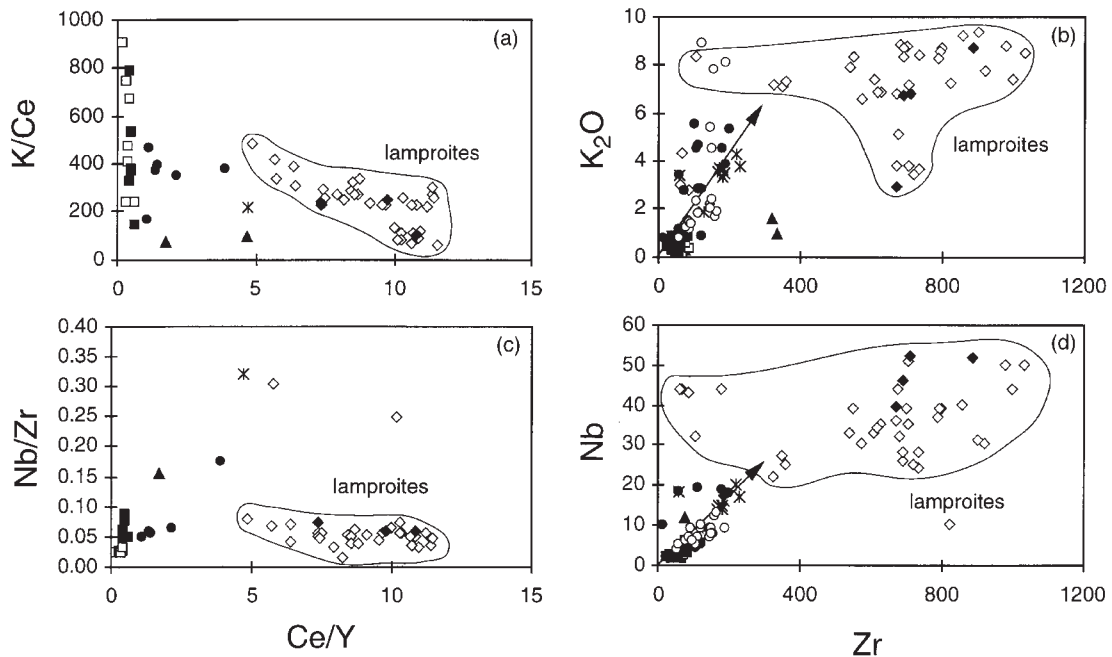


Fig. 12. Evidence for the role of minor residual phases during partial melting within the lithospheric mantle to produce the lamproites. The lamproites display a negative trend in K/Ce vs Ce/Y in (a) and K_2O remains relatively constant over a large range of Zr in (b) suggesting that K was compatible (in phlogopite) during partial melting. In contrast, the dykes and calc-alkaline volcanic rocks define a steep positive trend in (b) indicating similar incompatibility of K_2O and Zr. Similarly in (c) and (d), Nb/Zr forms a negative array against Ce/Y for the lamproites and Nb is relatively constant over a large range of Zr compared with the steep trend shown by the dykes and calc-alkaline volcanic rocks. This implies that Nb was compatible during partial melting, possibly in residual phlogopite (see text for discussion). Symbols and data sources as in Fig. 4.

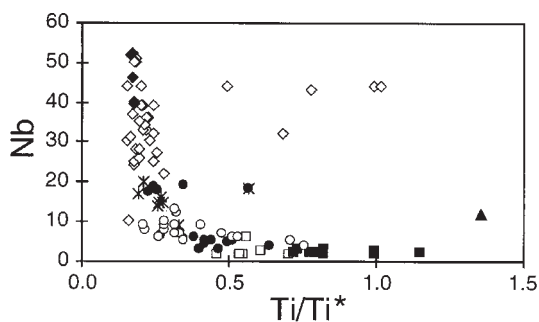


Fig. 13. Nb vs Ti/Ti^* (where Ti^* is the expected Ti concentration based on an interpolation between Zr and Y in Fig. 5d), showing that Nb concentrations increase as the size of the negative Ti anomaly increases; this implies that Nb is not being controlled by a residual Ti phase (e.g. rutile, ilmenite). Symbols and data sources as in Fig. 4.

enrichment as a means of generating the alkali basalt and even lamproite isotopic systematics, although some of the pyroxenites carrying this 'enriched' signature may well be younger (Pearson *et al.*, 1993).

Summary

Magmatism in the Betic-Alboran Domain was largely diffuse with the only sense of temporal and spatial migration being outward directed, as suggested by the

location of the lamproites lying to the north of the calc-alkaline rocks (Fig. 2). Magmatism appears to have commenced with shallow, decompression melting within the asthenosphere following removal of lithospheric mantle to produce a swarm of tholeiitic dykes. Subsequently, protracted eruption of calc-alkaline magmas appears to reflect increasing degrees of crustal contamination of similar, asthenosphere-derived magmas. Although it may not be possible to rule out a continental lithospheric mantle origin for the Malaga dykes and/or the calc-alkaline rocks, the geochemical data at hand do not demand such a source. One piece of evidence that may favour such an origin is the sub-chondritic Nb/Ta ratios that characterize both the dykes and calc-alkaline rocks and may reflect a melt-depleted lithospheric source. The calc-alkaline rocks were succeeded by crustal partial melts. Finally, alkali basalts and then lamproites formed by partial melting of enriched lithospheric mantle, some 4 my after the onset of calc-alkaline magmatism.

DISCUSSION IN THE CONTEXT OF RECENT GEODYNAMIC MODELS

The principal debate concerning the causes of extension in the Alboran Sea and surrounding areas now appears

to be between some form of back-arc extension driven by a retreating subduction zone (e.g. Lonergan & White, 1997), and some form of removal of lithosphere beneath an old contractional orogen (e.g. Platt & Vissers, 1989; Docherty & Banda, 1995; Carminati *et al.*, 1998). We will now combine the magmatic history of the Betic–Alboran Domain with other constraints in the context of these various competing geodynamic models.

Retreating subduction zone

The retreating subduction zone model (e.g. Lonergan & White, 1996) predicts a westward migrating volcanic arc showing a characteristic subduction-related geochemical signature. One of the great difficulties in interpreting the geochemistry of subduction-related rocks is distinguishing between the effects of sediment addition to the mantle source and those of shallow level, crustal contamination (e.g. Davidson, 1987). In the present case, although the main phase of magmatism in the Alboran Sea resembles that in island arcs, the development of the subduction signature appears to result from combined assimilation and fractional crystallization. In other words, features such as the negative Nb anomalies are not primary features that demand that the mantle source had been modified by subduction (see Fig. 10c). Furthermore, the geometry and timing of magmatism in no way suggests an island arc migrating behind a retreating subduction zone. For these reasons we feel that some form of lithospheric removal of lithosphere provides the best explanation for the syn- to post-extensional volcanism in the Alboran region, and this mechanism is most easily reconciled with the seismological evidence for detached bodies of cold mantle at depth (Grimison & Chen, 1986; Blanco & Spakman, 1993; Seber *et al.*, 1996).

Slab detachment

Slab detachment (Davies & von Blanckenburg, 1995) predicts a narrow, linear zone of magmatism and uplift that propagates along strike and is of limited extent. These magmas should be derived from the overlying lithosphere that was metasomatized during the preceding period of subduction, unless detachment occurs at a depth shallower than 50 km, in which case decompression melting of the asthenosphere is predicted (Davies & von Blanckenburg, 1995). This model seems inappropriate to the Betic–Alboran Domain on geometrical grounds. The pattern of magmatism and exhumation in this region does not define a linear zone and the magmatism is of considerable extent if the volcanic thicknesses in the Cabo de Gata region (~1000 m) are extrapolated beneath the Alboran Sea (Fig. 1). Also, the lithospheric mantle-derived magmas appear to be derived from ancient

enriched lithosphere (recall Nd model ages ~1.6–1.9 Ga), rather than one metasomatized during recent subduction. Thus, we do not find evidence to support the slab detachment model.

Delamination

Delamination of the lithospheric mantle (Bird, 1979) will bring hot asthenosphere into contact with the Moho. This should promote massive crustal melting and predicts a progressive migration of the resultant volcanism in the direction of delamination propagation. In the Betic–Alboran Domain, the only sense of migration to the magmatism is diffusely outwards from the Alboran Sea region (Fig. 2). Moreover, although unambiguous crustal melts do exist (e.g. the cordierite dacites), these are of small volume compared with the calc-alkaline volcanic rocks, which have a clear mantle component (see Fig. 10). Therefore, if massive crustal melting should be the hallmark of delamination, we find little evidence for it in the Betic–Alboran Domain.

Convective removal

Convective thinning of the lithospheric mantle (Houseman *et al.*, 1981) may produce an outward pattern of propagation of lithospheric melts rich in large ion lithophile and volatile elements (Turner *et al.*, 1992; Platt & England, 1994), depending on how much lithosphere has been removed. If a combination of the amount of thinning and any resultant extension raises the asthenosphere to within 50 km of the surface then decompression melting of the asthenosphere is predicted, with increasing amounts of crustal contamination of the asthenospheric melts as conductive and magmatic heating induces crustal melting.

It may not be possible to conclusively distinguish between the different mechanical and geometrical models for lithosphere removal using the geochemistry (but see discussion above), but for two reasons we will couch the remaining discussion in terms of the concept of convective thinning of the lithosphere, as originally proposed by Houseman *et al.* (1981), and recently elaborated by Houseman & Molnar (1997). The first is that the pattern of both extension and volcanism in the Alboran region is diffuse, lacking any obvious linear trend. The only suggestion of a temporal migration of activity is outwards: extension and magmatism started in early Miocene time in the Alboran Basin itself, whereas local extensional basins and volcanic centres developed within the peripheral Betic and Rif thrust belts to the north and south of the Alboran Domain in late Miocene and Pliocene time (Figs 1 and 2). This pattern is most easily reconciled with convective removal beneath the Alboran Domain,

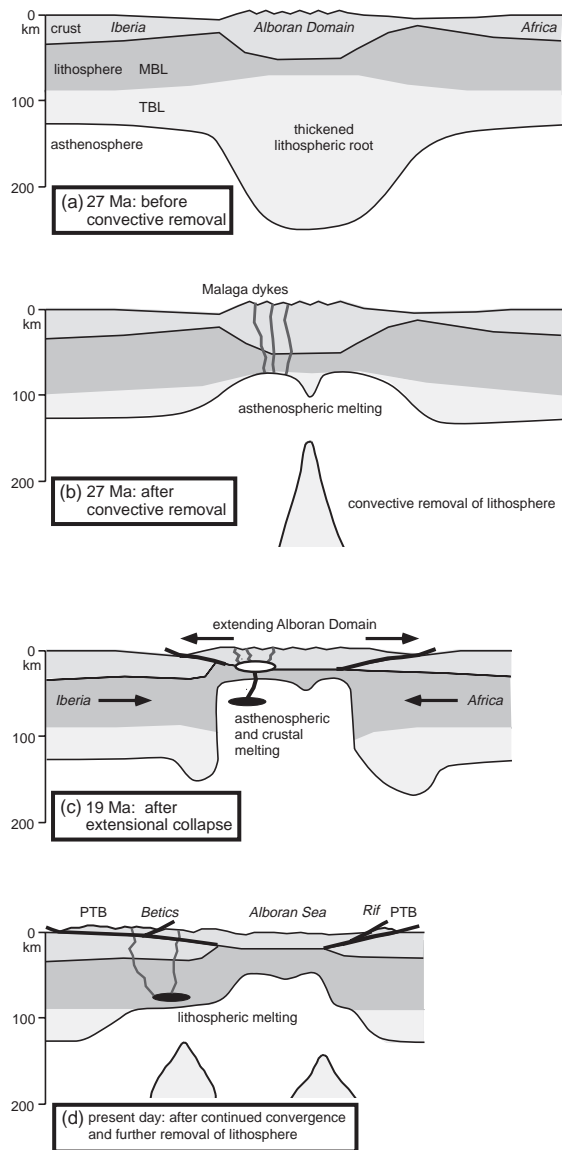


Fig. 14. Tectonic and magmatic evolution of the Betic–Alboran orogenic domain and its surroundings, shown in a series of N–S sections along the present-day 2°W meridian. Sections are true-scale, and the motions (after Platt & Vissers, 1989) are shown relative to the Iberian plate. (a) Section for ~27 Ma, after roughly homogeneous thickening of the Alboran crust and lithosphere. MBL, mechanical boundary layer; TBL, thermal boundary layer. The thermal boundary layer consists of lower lithospheric mantle with a low enough viscosity to be involved intermittently in convection. The position of the base of the MBL is speculative: we have taken into account the effects of radioactive heating of the overlying thickened crust (Platt *et al.*, 1998) and of total lithospheric thickness (Houseman & Molnar, 1997). (b) At ~27 Ma convective removal of lower lithospheric mantle results in decompression melting within the underlying asthenosphere and surface uplift. The resulting increase in the gravitational potential energy leads to extensional collapse of the Alboran Domain. (c) By 19 Ma the margins of the extending Alboran Domain have been thrust onto the adjacent Iberian and African continental margins. It should be noted that the main direction of extension was E–W, so that cross-sectional area is not conserved in this figure. Melting within the asthenosphere continues, and by 15 Ma these magmas have mixed with crustal melts

propagating outwards, possibly in response to the continued convergence between Africa and Iberia.

The second reason for favouring convective thinning is that the mechanism has a sound physical basis (Houseman *et al.*, 1981; Houseman & Molnar, 1997); the process is supported by observational evidence from the ocean basins (Parsons & McKenzie, 1978); and the thermal, mechanical, and magmatic consequences have been discussed in some detail (England & Houseman, 1989; Sandiford & Powell, 1990; Turner *et al.*, 1992; Zhou & Sandiford, 1992; Platt & England, 1994).

The magmatic record of the Betic–Alboran orogenic domain and its surroundings are shown in a series of N–S sections in Fig. 14. Convergent thickening in the Alboran Domain continued until ~40 Ma, resulting in a doubling of crustal thickness from ~30 to 60 km. Modelling of the P – T –time path experienced by rocks recovered on ODP Leg 161 from beneath the Alboran Sea (e.g. Platt *et al.*, 1998) suggests that extension started at ~30–27 Ma and was closely linked to intrusion of the Malaga dykes. These signify the onset of significant degrees (~10–15%) of decompression melting within the asthenosphere. Assuming upper mantle with a normal potential temperature of ~1280°C, partial melting will commence only if the asthenosphere is brought to within ~50 km of the surface (McKenzie & Bickle, 1988), consistent with the geochemical evidence that the Malaga dykes represent partial melting in the absence of residual garnet. Given the inferred crustal thicknesses, this requires that the lithospheric thickness was reduced to ~50 km by some combination of convective removal and stretching (Fig. 14b).

Removal of the dense lithospheric root beneath the orogen would result in major increases in elevation (~5 km) accompanied by increased gravitational potential energy and outwardly directed buoyancy forces (e.g. England & Houseman, 1989; Sandiford & Powell, 1990). A second response will be a rapid rise in temperature caused by placing hot asthenosphere close to the Moho (Fig. 14b). These predictions are substantiated by the P – T history of the metamorphic rocks recovered from beneath the Alboran Sea during ODP Leg 161. These record a rapid episode of decompression that was accompanied by heating of the order of 100°C at ~20–18 Ma (Soto & Platt, 1999; Soto *et al.*, 1999). There are two consequences. The first is that the strength of the

forming near the Moho to create the main phase of calc-alkaline volcanism. Continuing convergence of the Iberian and African plates causes further lithospheric thickening beneath the margins of the Alboran domain. (d) As Africa–Iberia convergence continues, laterally propagating convective removal of lithosphere causes lithospheric melting and alkaline to lamproitic volcanism on the margins of the orogen. PTB, peripheral thrust belts.

lithosphere will be greatly reduced such that the potential energy resulting from the elevation increases will lead to extensional collapse of the orogen (e.g. England & Houseman, 1989; Zhou & Sandiford, 1992) as illustrated in Fig. 14b and c. The second consequence is the onset of partial melting within the lower parts of the crust (Fig. 14c). The Malaga dykes provide evidence for interaction with the crust. The temporal evolution to calc-alkaline volcanism in which the crustal contribution is 20–50% and the subsequent eruption of cordierite–garnet dacites, which may represent 100% crustal melts, corroborates these predictions. In this context it should be recalled that there is evidence that much of the Alboran Sea is underlain by equivalents of the Cabo de Gata volcanic rocks (Comas *et al.*, 1999) and so the volume of these magmas may well be considerable (though poorly constrained, we estimate a minimum volume of 40 000 km³).

Removal of lithospheric mantle results in juxtaposition of hot asthenosphere against previously cooler lithospheric mantle (Fig. 14b). As noted by Turner *et al.* (1992, 1993, 1996a) and Platt & England (1994), any portions of the lithospheric mantle previously enriched by volatiles will have a lower solidus, relative to anhydrous asthenospheric peridotite, and will be likely to undergo partial melting upon heating by the newly juxtaposed asthenosphere. The likely rates of conductive heating suggest that this will occur on time-scales of 0–10 my (Turner *et al.*, 1996b) depending on the location of volatile-enriched portions in the lithospheric mantle relative to the amount removed. The lamproites clearly provide evidence for such magmatism. Moreover, the temporal progression from the Tallante alkali basalts, interpreted as being derived from the lower mechanical boundary layer of the lithospheric mantle, to the lamproites that were derived from shallower lithospheric mantle, which had undergone a previous melt extraction event, is consistent with progressive heating of the lithosphere from below. However, the emplacement of the alkali basalts and the lamproites post-dates the onset of asthenospheric and crustal-derived magmatism. It may be that older, lithosphere-derived rocks lie buried beneath the Alboran Sea calc-alkaline volcanic rocks, although this does not resolve the temporal evolution observed inland. Another possibility is suggested by the spatial restriction of the lamproites to regions inland of the calc-alkaline volcanic rocks (Figs 2 and 14d). The greater crustal thickness and elevation of the emergent part of the orogen suggests that it may be underlain by thicker lithosphere than the Alboran Sea, as a result of the emplacement of the northern part of the Alboran Domain onto the Iberian continental margin during the Miocene. If this is correct, it implies that limited convective removal of Iberian lithospheric mantle may have occurred during the late Miocene, leading to partial melting within the lower part

of the remaining lithospheric mantle and generation of the lamproites after the onset of calc-alkaline magmatism within the Alboran Domain. This is supported by the coincidence of the lamproite emplacement with a phase of uplift of this area which elevated marine Messinian to as much as 700 m above sea level. Thus, it would appear that early Miocene extension in the Alboran Sea region caused thrusting around its periphery, followed by outwardly propagating removal of lithospheric mantle. Finally, present-day lithospheric thicknesses beneath the Alboran Sea range from 40 to 90 km (Polyak *et al.*, 1996), suggesting that the lithosphere has rethickened by thermal accretion.

CONCLUSIONS

Magmatism in the Betic–Alboran Domain commenced with decompression melting within the asthenosphere following removal of lithospheric mantle to produce a swarm of tholeiitic dykes. Rapid rises in Moho temperature led to increasing degrees of crustal contamination and protracted eruption of calc-alkaline magmas succeeded by crustal partial melts. Emplacement of alkali basalts followed by lamproites, formed by partial melting of sediment-enriched lithospheric mantle, some 4 my after the onset of calc-alkaline magmatism, records the vertical progression of partial melting through the lithospheric mantle as convective removal propagated outwards in the orogen. The general cessation of magmatism at ~6 Ma presumably reflects cooling and rethickening of the lithospheric mantle, and this is supported by heat flow data, which suggest that present-day lithospheric thicknesses beneath the Alboran Sea range from 40 km in the centre to 90 km at the periphery (Polyak *et al.*, 1996).

Thermal modelling of metamorphic rocks recovered from the basement beneath the Alboran Sea (Platt *et al.*, 1998), as well as the magmatic constraints presented here, both suggest that the majority of the lithospheric mantle was removed at ~30–27 Ma. Nevertheless, the alkali basalts and lamproites attest to the presence of some remaining, ancient, lithospheric mantle, at least beneath the Iberian crust at the margins of the Alboran Sea, at 10–7 Ma. We suggest that the combined magmatic, structural and metamorphic record argues against geodynamic models invoking retreating subduction, slab detachment or delamination of the entire lithospheric mantle at the Moho. Rather, convective removal (e.g. Houseman *et al.*, 1981; Houseman, 1996) may be a more appropriate process.

ACKNOWLEDGEMENTS

We are particularly grateful to Nigel Harris, Nick Rogers, Dan McKenzie and Phil England for their helpful comments and discussions. Thanks also go to Peter van

Calsteren, Mabs Gilmour and Jessica Bartlett for their assistance with the isotope analyses, and to Chris Ottley for help with the ICP-MS analyses. The manuscript was significantly improved by helpful reviews from George Jenner, Scott Baldridge, Claudia Lewis and an anonymous reviewer, as well as the editorial expertise of Jon Davidson. Field work was funded by NERC Grant GR3/10828 to J.P.P., and S.T. is supported by a Royal Society Research Fellowship.

REFERENCES

- Allerton, S., Lonergan, L., Platt, J. P., Platzman, E. S. & McClelland, E. (1993). Palaeomagnetic rotations in the eastern Betic Cordillera, southern Spain. *Earth and Planetary Science Letters* **119**, 225–241.
- Ancochea, E. & Nixon, P. H. (1987). Xenoliths in the Iberian Peninsula. In: Nixon, P. H. (ed.) *Mantle Xenoliths*. New York: John Wiley, pp. 119–125.
- Argles, T. W., Platt, J. P. & Waters, D. J. (1999). Attenuation and excision of a crustal section during extensional exhumation: the Carratraca Massif, Betic Cordillera, Southern Spain. *Journal of the Geological Society, London* **156**, 149–162.
- Banda, E., Udias, A., Mueller, S., Mezcuca, J., Boloix, M., Qallart, J. & Aparicio, A. (1983). Crustal structure beneath Spain from deep seismic sounding experiments. *Physics of Earth and Planetary Interiors* **31**, 277–280.
- Bellon, H., Bordet, P. & Montenat, C. (1983). Chronologie du magmatisme néogène des Cordillères bétiques (Espagne méridionale). *Bulletin de la Société Géologique de France* **25**, 205–217.
- Bird, P. (1979). Continental delamination and the Colorado Plateau. *Journal of Geophysical Research* **84**, 7561–7571.
- Blanco, M. J. & Spakman, W. (1993). The P-wave velocity structure of the mantle below the Iberian Peninsula: evidence for subduction lithosphere below southern Spain. *Tectonophysics* **221**, 13–34.
- Carminati, E., Wortel, M. J. R., Spakman, W. & Sabadini, R. (1998). The role of slab detachment processes in the opening of the western-central Mediterranean basins: some geological and geophysical evidence. *Earth and Planetary Science Letters* **160**, 651–665.
- Comas, M. C., Zahn, R., Klaus, A., *et al.* (1996). Initial reports. *Proceedings of the Ocean Drilling Program, Initial Reports*. College Station, TX: Ocean Drilling Program, 1023 pp.
- Comas, M. C., Platt, J. P., Soto, J. I. & Watts, A. B. (1999). The origin and history of the Alboran Basin, insights from ODP Leg 161 results (Western Mediterranean). In: Zahn, R., Comas, M. C. & Klaus A. (eds) *Proceedings of the Ocean Drilling Program, Scientific Results, 161*. College Station, TX: Ocean Drilling Program (in press).
- Davidson, J. P. (1987). Crustal contamination versus subduction zone enrichment: examples from the Lesser Antilles and implications for mantle source compositions of island arc volcanic rocks. *Geochimica et Cosmochimica Acta* **51**, 2185–2198.
- Davies, J. H. & von Blanckenburg, F. (1995). Slab breakoff: a model of lithospheric detachment and its test in the magmatism and deformation of collisional orogens. *Earth and Planetary Science Letters* **129**, 85–102.
- DePaolo, D. J. (1981). Trace element and isotopic effects of combined wallrock assimilation and fractional crystallisation. *Earth and Planetary Science Letters* **53**, 189–202.
- Di Battistini, G., Toscani, L., Iaccarino, S. & Villa, I. M. (1987). K/Ar ages and the geological setting of calc-alkaline volcanic rocks from Sierra de Gata, SE Spain. *Neues Jahrbuch für Mineralogie, Monatshefte* **8**, 369–383.
- Docherty, C. & Banda, E. (1995). Evidence for eastward migration of the Alboran Sea based on regional subsidence analysis: a case for basin formation by delamination of the subcrustal lithosphere? *Tectonics* **14**, 804–818.
- Edgar, A. D., Green, D. H. & Hibberson, W. O. (1976). Experimental petrology of a highly potassic magma. *Journal of Petrology* **17**, 339–356.
- Ellam, R. M. & Cox, K. G. (1991). An interpretation of Karoo picrite basalts in terms of interaction between asthenospheric magmas and the mantle lithosphere. *Earth and Planetary Science Letters* **105**, 330–342.
- England, P. C. & Houseman, G. A. (1989). Extension during continental convergence, with application to the Tibetan Plateau. *Journal of Geophysical Research* **94**, 17561–17579.
- García-Dueñas, V., Balanyá, J. C. & Martínez-Martínez, J. M. (1992). Miocene extensional detachments in the outcropping basement of the Northern Alboran Basin (Betics) and their tectonic implications. *Geomarine Letters* **12**, 88–95.
- Grimison, N. L. & Chen, W. P. (1986). The Azores–Gibraltar plate boundary: focal mechanisms, depths of earthquakes, and their tectonic implications. *Journal of Geophysical Research* **91**, 2029–2047.
- Guezou, J. C., Frizon de Lamotte, D., Coulon, M. & Morel, J.-L. (1991). Structure and kinematics of the Prebetic nappe complex (southern Spain): definition of a ‘Betic Floor Thrust’ and implications in the Betic–Rif orocline. *Annales Tectonicae* **5**, 32–48.
- Halliday, A. N., Lee, C.-C., Tommasini, S., Davies, G. R., Paslick, C. R., Fitton, J. G. & James, D. E. (1995). Incompatible trace elements in OIB and MORB and source enrichment in the sub-oceanic mantle. *Earth and Planetary Science Letters* **133**, 379–395.
- Hart, S. R. (1984). A large-scale isotope anomaly in the Southern Hemisphere mantle. *Nature* **309**, 753–757.
- Hawkesworth, C. J., Kempton, P. D., Rogers, N. W., Ellam, R. M. & van Calsteren, P. W. (1990). Continental mantle lithosphere, and shallow level enrichment processes in the Earth’s mantle. *Earth and Planetary Science Letters* **96**, 256–268.
- Hergt, J. M., Chappell, B. W., McCulloch, M. T., McDougall, I. & Chivas, A. R. (1989). Geochemical and isotopic constraints on the origin of the Jurassic dolerites of Tasmania. *Journal of Petrology* **30**, 841–883.
- Houseman, G. A. (1996). From mountains to basin. *Nature* **379**, 771–772.
- Houseman, G. A. & Molnar, P. (1997). Gravitational (Rayleigh–Taylor) instability of a layer with non-linear viscosity and convective thinning of continental lithosphere. *Geophysical Journal International* **128**, 125–150.
- Houseman, G. A., McKenzie, D. P. & Molnar, P. J. (1981). Convective instability of a thickened boundary layer and its relevance for the thermal evolution of continental convergent belts. *Journal of Geophysical Research* **86**, 6115–6132.
- Ionov, D. A. & Hofmann, A. W. (1995). Nb–Ta-rich mantle amphiboles and micas: implications for subduction-related metasomatic trace element fractionations. *Earth and Planetary Science Letters* **131**, 341–356.
- Kelley, S. P. (1995). Ar–Ar dating by laser microprobe. In: Potts, P. J., Bowens, J. F. N. & Reed, S. J. B. (eds) *Microanalytical Techniques in the Geosciences*. London: Chapman and Hall, pp. 326–358.
- Kelley, S. P. & Platt, J. P. (1999). Ar–Ar dating of biotite and muscovite from Alboran basement samples, ODP Site 976. In: Comas, M. C., Zahn, R. & Klaus, A. (eds) *Proceedings of the Ocean Drilling Program, Scientific Results, 161*. College Station, TX: Ocean Drilling Program (in press).
- Kirker, A. I. & Platt, J. P. (1998). Unidirectional slip vectors in the western Betic Cordillera: implications for the formation of the Gibraltar arc. *Journal of the Geological Society, London* **155**, 193–208.
- Klein, E. M. & Langmuir, C. H. (1987). Global correlations of ocean ridge basalt chemistry with axial depth and crustal thickness. *Journal of Geophysical Research* **92**, 8089–8115.

- Kumar, N., Reisberg, L. & Zindler, A. (1996). A major and trace element and Sr, Nd and Os isotopic study of a thick pyroxenite layer from the Beni Bousera ultramafic complex of N. Morocco. *Geochimica et Cosmochimica Acta* **60**, 1429–1444.
- Loneragan, L. & White, N. (1997). Origin of the Betic–Rif mountain belt. *Tectonics* **16**, 504–522.
- Loneragan, L., Platt, J. P. & Gallagher, L. (1994). The Internal–External Zone boundary in the eastern Betic Cordillera, SE Spain. *Journal of Structural Geology* **16**, 175–188.
- Mahnes, G., Minster, J. F. & Allègre, C. J. (1978). Comparative uranium–thorium–lead and rubidium–strontium study of the Saint Severin amphoterite: consequences for early solar system chronology. *Earth and Planetary Science Letters* **39**, 14–24.
- McKenzie, D. (1989). Some remarks on the movement of small melt fractions in the mantle. *Earth and Planetary Science Letters* **95**, 53–72.
- McKenzie, D. P. & Bickle, M. J. (1988). The volume and composition of melt generated by extension of the lithosphere. *Journal of Petrology* **29**, 625–679.
- Mengel, K. & Green, D. H. (1989). Stability of amphibole and phlogopite in metasomatised peridotite under water-saturated and water-undersaturated conditions. In: J. Ross (ed.) *Kimberlites and Related Rocks, Vol. 1. Geological Society of Australia Special Publication* **14**, 571–581.
- Monié, P., Torres-Roldán, R.-L. & García-Casco, A. (1994). Cooling and exhumation of the western Betic Cordilleras, $^{40}\text{Ar}/^{39}\text{Ar}$ thermochronological constraints on a collapsed terrane. *Tectonophysics* **238**, 353–379.
- Munksgaard, N. C. (1984). High $\delta^{18}\text{O}$ and possible pre-eruptional Rb–Sr isochrons in cordierite-bearing Neogene volcanics from SE Spain. *Contributions to Mineralogy and Petrology* **87**, 351–358.
- Nelson, D. R., McCulloch, M. T. & Sun, S.-S. (1986). The origins of ultrapotassic rocks as inferred from Sr, Nd and Pb isotopes. *Geochimica et Cosmochimica Acta* **50**, 231–245.
- Nixon, P. H., Thirlwall, M. F., Buckley, F. & Davies, C. J. (1984). Spanish and Western Australian lamproites: aspects of whole rock geochemistry. In: Kornprobst, J. (ed.) *Kimberlites and Related Rocks*. Amsterdam: Elsevier, pp. 285–296.
- Parsons, B. & McKenzie, D. (1978). Mantle convection and the thermal structure of the plates. *Journal of Geophysical Research* **83**, 4485–4496.
- Pearson, D. G., Davies, G. R., Nixon, P. H., Greenwood, P. B. & Matthey, D. P. (1991). Oxygen isotope evidence for the origin of pyroxenites in the Beni Bousera peridotite massif, N. Morocco: derivation from subducted oceanic lithosphere. *Earth and Planetary Science Letters* **102**, 289–301.
- Pearson, D. G., Davies, G. R. & Nixon, P. H. (1993). Geochemical constraints on the petrogenesis of diamond facies pyroxenites from the Beni Bousera peridotite massif, north Morocco. *Journal of Petrology* **34**, 125–172.
- Plank, T. & White, W. M. (1995). Nb and Ta in arc and mid-ocean ridge basalts. *EOS Transactions, American Geophysical Union* **76**, 655.
- Platt, J. P. & England, P. C. (1994). Convective removal of lithosphere beneath mountain belts: thermal and mechanical consequences. *American Journal of Science* **294**, 307–336.
- Platt, J. P. & Vissers, R. L. M. (1989). Extensional collapse of thickened continental lithosphere: a working hypothesis for the Alboran Sea and Gibraltar arc. *Geology* **17**, 540–543.
- Platt, J. P., Allerton, S., Kirker, A. & Platzman, E. S. (1995). Origin of the western Subbetic arc, southern Spain: palaeomagnetic and structural evidence. *Journal of Structural Geology* **17**, 765–775.
- Platt, J. P., Soto, I. J., Comas, M. C. & Leg 161 Shipboard Scientists (1996). Decompression and high-temperature–low-pressure metamorphism in the exhumed floor of an extensional basin, Alboran Sea, western Mediterranean. *Geology* **24**, 447–450.
- Platt, J. P., Soto, I. J., Whitehouse, M. J., Hurford, A. J. & Kelley, S. P. (1998). Thermal evolution, rate of exhumation, and tectonic significance of metamorphic rocks from the floor of the Alboran extensional basin, western Mediterranean. *Tectonics* **17**, 671–689.
- Platzman, E. S. (1992). Paleomagnetic rotations and the kinematics of the Gibraltar arc. *Geology* **20**, 311–314.
- Platzman, E. S., Platt, J. P. & Olivier, P. (1993). Palaeomagnetic rotations and fault kinematics in the Rif arc of Morocco. *Journal of the Geological Society, London* **150**, 707–718.
- Polyak, B. G., Fernández, M., Khutorskoy, M. D., Soto, J. I., Basov, I. A., Comas, M. C., Khain, V. Ye., Alonso, B., Agapova, G. V., Mazurova, I. S., Negrodo, A., Tochitsky, V. O., de la Linde, J., Bogdanov, N. A. & Banda, E. (1996). Heat flow in the Alboran Sea, western Mediterranean. *Tectonophysics* **263**, 191–218.
- Potts, P. J., Webb, P. C. & Watson, J. S. (1984). Energy dispersive X-ray fluorescence analysis of silicate rocks for major and trace elements. *X-Ray Spectrometry* **13**, 2–15.
- Priem, H. N. A., Hebeda, E. H., Boelrijk, N. A. I. M., Verdurmen, T. & Oen, I. S. (1979). Isotopic dating of the emplacement of the ultramafic masses in the Serrania de Ronda, southern Spain. *Contributions to Mineralogy and Petrology* **61**, 103–109.
- Reisberg, L. & Zindler, A. (1986). Extreme isotopic variations in the upper mantle: evidence from Ronda. *Earth and Planetary Science Letters* **81**, 29–45.
- Richard, P., Shimizu, N. & Allègre, C. J. (1976). $^{143}\text{Nd}/^{144}\text{Nd}$, a natural tracer: an application to oceanic basalts. *Earth and Planetary Science Letters* **31**, 269–278.
- Royden, L. H. (1993). Evolution of retreating subduction boundaries formed during continental collision. *Tectonics* **12**, 629–638.
- Sandiford, M. & Powell, R. (1990). Some isostatic and thermal consequences of the vertical strain geometry in convergent orogens. *Earth and Planetary Science Letters* **95**, 85–96.
- Seber, D., Barazangi, M., Ibenbrahim, A. & Demnati, A. (1996). Geophysical evidence for lithospheric delamination beneath the Alboran Sea and Rif–Betic mountains. *Nature* **379**, 785–790.
- Soto, J. I. & Platt, J. P. (1999). Petrological and structural evolution of high-grade metamorphic rocks from the floor of the Alboran Sea basin, Western Mediterranean. *Journal of Petrology* **40**, 21–60.
- Soto, J. I., Platt, J. P., Sánchez-Gómez, M. & Azañón, J. M. (1999). PT evolution of the metamorphic basement of the Alboran Sea (site 976) based on thermobarometry and structural observations. In: Comas, M. C., Zahn, R. & Klaus, A. (eds) *Proceedings of the Ocean Drilling Program, Scientific Results, 161*. College Station, TX: Ocean Drilling Program (in press).
- Sun, S.-s. & McDonough, W. F. (1989). Chemical and isotopic systematics of oceanic basalts: implications for mantle composition and processes. In: Saunders, A. D. & Norry, M. J. (eds) *Magmatism in Ocean Basins. Geological Society, London, Special Publication* **42**, 313–345.
- Torres-Roldán, R. L., Poli, G. & Peccerillo, A. (1986). An Early Miocene arc–tholeiitic dike event from the Alboran Sea—evidence for precollisional subduction and back-arc crustal extension in the westernmost Mediterranean. *Geologische Rundschau* **75**, 219–234.
- Turner, S., Hawkesworth, C. J., Liu, J., Rogers, N., Kelley, S. & van Calsteren, P. (1993). Timing of Tibetan uplift constrained by analysis of volcanic rocks. *Nature* **364**, 50–53.
- Turner, S. & Hawkesworth, C. (1995). The nature of the sub-continental mantle: constraints from the major element composition of continental flood basalts. *Chemical Geology* **120**, 295–314.
- Turner, S., Arnaud, N., Liu, J., Harris, N., Hawkesworth, J., Kelley, S., Rogers, N., van Calsteren, P. & Deng, W. (1996a). Post-collision, shoshonitic volcanism on the Tibetan Plateau: implications for convective thinning of the lithosphere and the source of ocean island basalts. *Journal of Petrology* **37**, 45–71.

- Turner, S., Hawkesworth, C., Gallagher, K., Stewart, K., Peate, D. & Mantovani, M. (1996b). Mantle plumes, flood basalts, and thermal models for melt generation beneath continents: assessment of a conductive heating model and application to the Paraná. *Journal of Geophysical Research* **101**, 11503–11518.
- Turner, S. P., Sandiford, M. & Foden, J. D. (1992). Some geodynamic and compositional constraints on 'post orogenic' magmatism. *Geology* **20**, 931–934.
- Van der Wal, D. & Vissers, R. L. M. (1993). Uplift and emplacement of upper mantle rocks in the western Mediterranean. *Geology* **21**, 1119–1122.
- Venturelli, G., Capedri, S., Di Battistini, G., Crawford, A., Kogarko, L. N. & Celestini, S. (1984). The ultrapotassic rocks from southeastern Spain. *Lithos* **17**, 37–54.
- Venturelli, G., Mariani, E. S., Foley, S. F., Capedri, S. & Crawford, A. (1988). Petrogenesis and conditions of crystallization of Spanish lamproitic rocks. *Canadian Mineralogist* **26**, 67–79.
- Vissers, R. L. M., Platt, J. P. & van der Wal, D. (1995). Late orogenic extension of the Betic Cordillera and the Alboran Domain: a lithospheric view. *Tectonics* **14**, 786–803.
- Zhou, S. & Sandiford, M. (1992). On the stability of isostatically compensated mountain belts. *Journal of Geophysical Research* **97**, 14207–14223.

APPENDIX

Table A1: $^{40}\text{Ar}/^{39}\text{Ar}$ isotope data and calculated ages for Betic magmatic rocks

Sample	$^{40}\text{Ar}/^{39}\text{Ar}$	$^{38}\text{Ar}/^{39}\text{Ar}$	$^{37}\text{Ar}/^{39}\text{Ar}$	$^{36}\text{Ar}/^{39}\text{Ar}$	^{39}Ar	$^{40}\text{Ar}^*/^{39}\text{Ar}$	Age (Ma)	\pm
B304 biotite								
1	2.374	0.015	n.d.	0.0021	118.9	1.757	10.1	0.3
2	2.373	0.015	n.d.	0.0015	38.0	1.939	11.2	0.7
3	4.639	0.018	n.d.	0.0090	119.0	1.990	11.5	0.6
Weighted mean							10.5	0.4
B312 wr								
1	2.641	0.015	n.d.	0.0030	53.3	1.767	10.2	0.6
2	24.121	0.038	n.d.	0.0760	126.9	1.675	9.7	3.9
3	58.123	0.056	n.d.	0.1162	34.5	23.792	132.8	12.7
4	26.971	0.040	n.d.	0.0584	72.0	9.708	55.4	7.3
Weighted mean							10.7	3.7
B321 biotite								
1	1.467	0.016	n.d.	0.0014	157.7	1.067	6.2	0.4
2	1.544	0.014	0.11	0.0017	116.8	1.043	6.0	0.4
3	1.765	0.015	1.72	0.0024	98.9	1.059	6.1	0.5
4	1.155	0.018	1.15	0.0002	106.8	1.105	6.4	0.4
Weighted mean							6.2	0.1
B305 wr								
1	2.042	0.013	0.50	0.0029	193.5	1.190	6.9	0.2
2	1.380	0.013	0.72	0.0009	171.2	1.102	6.4	0.2
3	1.738	0.013	2.41	0.0002	88.7	1.688	9.7	0.6
Weighted mean							6.8	0.5
B303 bioite								
1	1.759	0.020	0.85	0.0014	33.6	1.345	7.8	0.7
2	2.600	0.018	0.20	0.0037	165.1	1.496	8.6	0.2
3	2.026	0.018	0.43	0.0022	207.8	1.379	8.0	0.2
4	2.322	0.018	1.55	0.0025	50.6	1.585	9.2	0.8
5	3.818	0.018	1.47	0.0073	61.2	1.660	9.6	0.8
Weighted mean							8.3	0.2
B309 biotite								
1	1.682	0.018	0.20	0.0014	383.1	1.263	7.3	0.1
2	1.459	0.018	0.26	0.0006	344.2	1.281	7.4	0.2
3	8.845	0.024	0.64	0.0262	68.3	1.117	6.5	0.8
4	2.813	0.018	1.19	0.0058	39.5	1.114	6.4	0.9
5	1.574	0.018	0.26	0.0010	133.1	1.277	7.4	0.3
Weighted mean							7.3	0.1
B320 wr								
1	2.980	0.018	0.35	0.0041	99.0	1.765	10.2	0.3
2	6.105	0.041	14.08	0.0157	8.4	1.453	8.4	5.1
3	3.369	0.039	6.01	0.0049	52.0	1.927	11.1	0.9
4	4.261	0.026	7.54	0.0082	73.2	1.850	10.7	0.7
Weighted mean							10.4	0.2
B301 biotite								
1	4.178	0.020	0.05	0.0090	145.4	1.511	8.7	0.4
2	3.075	0.020	0.44	0.0054	283.9	1.474	8.5	0.2
3	1.626	0.018	0.34	0.0005	292.8	1.479	8.5	0.1
4	1.628	0.019	0.37	0.0007	205.5	1.422	8.2	0.2
5	1.703	0.019	0.41	0.0005	463.3	1.550	9.0	0.1
6	3.917	0.020	0.28	0.0086	733.5	1.389	8.0	0.2
7	2.510	0.019	0.46	0.0036	435.6	1.435	8.3	0.2
Weighted mean							8.5	0.1

Table A1: *continued*

Sample	$^{40}\text{Ar}/^{39}\text{Ar}$	$^{38}\text{Ar}/^{39}\text{Ar}$	$^{37}\text{Ar}/^{39}\text{Ar}$	$^{36}\text{Ar}/^{39}\text{Ar}$	^{39}Ar	$^{40}\text{Ar}^*/^{39}\text{Ar}$	Age (Ma)	\pm
B311 amph								
1	5.457	0.064	16.94	0.0154	12.9	0.897	5.2	2.8
2	5.314	0.058	13.56	0.0128	32.9	1.541	8.9	2.3
3	2.457	0.040	9.25	0.0027	44.9	1.658	9.6	1.2
4	2.344	0.043	11.12	0.0026	26.0	1.587	9.2	1.4
Weighted mean							9.0	0.7
B318 amph								
1	2.505	0.017	0.92	0.0006	63.5	2.342	13.5	0.4
2	2.934	0.024	2.95	0.0020	143.9	2.337	13.5	0.3
3	3.787	0.033	7.05	0.0056	79.2	2.142	12.4	0.8
Weighted mean							13.4	0.2
B322 wr								
1	34.448	0.039	9.16	0.1053	39.7	3.340	19.2	1.5
2	40.853	0.045	13.07	0.1375	35.4	0.225	1.3	3.1
3	21.411	0.026	7.28	0.0653	158.9	2.119	12.2	2.0
4	21.793	0.049	63.09	0.0694	4.2	1.282	7.4	8.0
Weighted mean							14.6	3.5
B323 wr								
1	33.513	0.037	9.13	0.0933	29.8	5.954	34.2	1.5
2	26.562	0.032	7.27	0.0700	49.8	5.882	33.7	2.2
3	25.006	0.033	11.70	0.0721	23.1	3.698	21.3	2.5
4	18.989	0.028	7.14	0.0495	62.2	4.359	25.1	0.9
Weighted mean							27.7	2.6
M7A step heat								
M7A-7 1	-12.528	0.083	9.71	-0.0842	-0.1	12.349	137.2	183.6
M7A-7 2	314.485	0.535	4.22	0.9760	6.7	26.076	278.4	27.9
M7A-7 3	31.941	0.279	9.64	0.0830	10.9	7.408	83.6	4.7
M7A-7 4	16.953	0.309	3.22	0.0471	32.8	3.044	34.8	1.4
M7A-7 5	9.793	0.157	2.02	0.0250	18.4	2.396	27.5	1.7
M7A-7 6	7.321	0.113	1.34	0.0153	21.5	2.810	32.2	1.0
M7A-7 7	6.279	0.128	2.29	0.0113	25.7	2.930	33.5	0.8
M7A-7 8	6.387	0.083	1.50	0.0128	40.0	2.597	29.7	0.8
M7A-7 9	8.250	0.074	1.49	0.0195	30.5	2.476	28.4	1.0
M7A-7 10	9.760	0.076	1.52	0.0235	39.0	2.819	32.3	0.6
M7A-7 11	12.618	0.078	1.67	0.0313	23.2	3.373	38.5	1.4
M7A-7 12	13.339	0.090	2.07	0.0356	11.5	2.815	32.2	1.8
M7A-7 13	19.657	0.104	2.44	0.0505	20.3	4.743	53.9	1.0
Total gas age							37.6	0.9
Plateau isochron							30.2	0.9
M7B step heat								
M7B-4 1	2.907	0.107	2.43	0.0064	12.5	1.014	11.7	1.1
M7B-4 2	3.047	0.112	2.07	0.0047	26.7	1.671	19.2	0.8
M7B-4 3	2.703	0.044	1.06	0.0029	31.7	1.845	21.2	0.6
M7B-4 4	2.929	0.048	1.45	0.0041	34.9	1.728	19.8	0.6
M7B-4 5	3.743	0.063	1.92	0.0079	53.4	1.405	16.2	0.6
M7B-4 6	3.094	0.050	1.73	0.0066	41.3	1.156	13.3	0.8
M7B-4 7	4.403	0.049	2.54	0.0095	136.9	1.599	18.4	0.3
M7B-4 8	30.237	0.331	8.43	0.0977	77.6	1.354	15.6	2.5
M7B-4 9	14.461	0.233	6.19	0.0237	5.5	7.465	84.2	3.6
M7B-4 10	25.355	0.346	9.07	0.0820	44.5	1.115	12.8	1.6
M7B-4 11	9.510	0.267	5.68	0.0230	4.8	2.717	31.1	4.2
M7B-4 12	9.466	0.249	6.08	0.0301	6.5	0.583	6.7	3.1
M7B-4 13	9.801	0.309	7.60	0.0199	7.5	3.935	44.9	4.2
M7B-4 14	11.439	0.294	7.82	0.0306	5.9	2.393	27.4	3.4
M7B-4 15	12.497	0.306	10.17	0.0349	27.5	2.188	25.1	0.7
M7B-4 16	18.789	0.197	13.36	0.0538	35.4	2.882	33.0	1.7
Total gas age							19.1	0.4
Plateau isochron							17.7	0.3

n.d., not determined.

Table A2: Additional data for Betic volcanics and Malaga dykes

Sample:	M6	M8	M4	B323	M10	M7	B301	B301a	B303	B315	B314	B311	B317	B320	B312	B309a*	B315a	B305	B304
Locality	Malaga	Malaga	Malaga	Malaga	Malaga	Malaga	Mazarrón	Mazarrón	Mazarrón	C. de Gata	C. de Gata	C. de Gata	C. de Gata	C. de Gata	C. de Gata	C. de Gata	C. de Gata	Jumilla	Tallante
Latitude (°N):	36°52'	36°50'	36°49'	36°51'	36°46'	36°52'	37°36'	37°36'	37°36'	36°47'	36°51'	37°01'	36°47'	36°52'	36°55'	37°14'	36°47'	38°27'	37°40'
Longitude (°W):	4°26'	4°27'	4°26'	4°27'	4°26'	4°26'	1°17'	1°17'	1°21'	2°07'	2°03'	1°53'	2°07'	2°10'	2°03'	1°50'	2°07'	1°27'	1°09'
SiO ₂ (wt %)	51.87	52.75	53.19	53.48	53.49	56.73	63.82	67.19	70.92	58.18	59.76	59.84	60.73	62.48	62.83	29.63	67.21	50.62	46.16
TiO ₂	0.78	0.73	0.80	0.86	0.84	1.00	0.56	0.56	0.61	0.67	0.63	0.45	0.61	0.52	0.38	1.71	0.56	1.32	2.43
Al ₂ O ₃	16.62	15.88	16.42	16.34	16.15	15.78	15.52	15.75	11.80	16.81	15.39	15.73	15.92	16.00	15.20	6.73	14.07	8.94	17.66
Fe ₂ O ₃	8.55	8.44	8.62	9.17	8.87	9.42	4.64	2.98	2.75	6.49	6.44	5.27	5.80	5.40	3.70	36.30	3.89	6.41	10.12
MnO	0.15	0.15	0.15	0.19	0.15	0.14	0.07	0.03	0.03	0.11	0.28	0.06	0.11	0.08	0.05	1.97	0.05	0.09	0.17
MgO	7.36	5.25	6.16	5.48	5.07	4.05	2.30	1.77	1.28	3.84	2.23	3.42	4.81	3.09	2.08	2.09	0.43	15.18	5.16
CaO	10.86	9.33	10.07	9.35	9.33	6.67	2.83	2.70	2.04	7.61	5.39	5.72	3.80	4.75	4.85	5.06	0.53	4.62	8.70
Na ₂ O	2.59	2.79	2.76	2.46	2.99	3.60	2.25	2.31	1.39	2.54	1.12	2.26	2.23	2.35	2.47	1.00	0.26	0.85	4.34
K ₂ O	0.36	0.54	0.24	0.56	0.46	0.86	3.89	4.49	5.36	0.85	5.53	2.79	2.85	2.83	4.49	0.92	11.43	6.74	0.92
P ₂ O ₅	0.07	0.08	0.08	0.09	0.08	0.11	0.35	0.36	0.34	0.15	0.11	0.10	0.15	0.13	0.09	0.15	0.14	1.60	1.13
LOI	1.41	3.56	1.65	1.94	2.26	1.50	3.23	1.50	1.94	2.40	3.04	4.46	3.27	2.40	3.90	-3.40	1.03	2.53	3.39
Total	100.62	99.50	100.14	99.92	99.69	99.86	99.46	99.64	98.46	99.65	99.92	100.10	100.28	100.03	100.04	82.16	99.60	98.90	100.18
Rb (ppm)	14.9	30.9	9.9	27.2	22.9	37.6	223.5	220	199	32.2	324	88.9	144	150	149	46.9	474	347	74.4
Sr	144	208	176	174	167	195	383.1	404	521	441	218	131	202	159	108	4063	44.7	1001	1156
Y	18.9	18.7	18.6	18.6	21	23.6	25.7	22.1	18.4	18.7	17.6	11.6	17.4	17.4	16	0	13.1	31.8	29.3
Zr	50	57	56	61	56	81	187	180	199	119	103	70	121	111	107	134	105	693	334
Nb	1.6	2	2.2	3.1	2.2	3.1	17.5	18.7	17.9	5.2	5.3	3.2	5.9	5.5	6.7	12.5	4.4	46.2	93.7
Ba	57	86	52	105	57	96	1089	1119	6541	328	1102	288	269	260	303	19112	1116	2781	1313
Pb	4	1	2	2	1	3	89	83	61	32	38	35	38	15	29	16893	30	175	12
Th	0	2	3	1	0	4	39	36	40	7	5	5	9	7	14	121	8	115	32
U	0	1	2	0	1	4	18	10	10	4	3	3	5	5	4	13	3	27	5
Sc	40	37	39	36	33	32	17	12	12	26	26	21	21	22	13	1	17	18	18
V	239	243	241	258	265	307	105	107	91	182	157	138	149	117	72	0	141	106	232
Cr	44	32	58	29	15	12	86	87	107	35	45	31	34	35	26	11	30	851	80
Co	37	30	34	32	32	23	14	9	8	17	16	11	18	12	8	0	6	50	34
Ni	42	23	28	19	18	10	26	25	26	9	11	12	8	10	7	49	5	682	83
Cu	57	58	52	97	8	52	23	24	14	20	13	7	38	18	18	357	11	51	31
Zn	62	62	50	58	45	65	58	38	32	61	221	56	60	59	42	22655	249	79	112
Ga	16	15	17	17	16	18	21	19	12	21	16	17	21	18	16	13	13	16	24

*Sample B309a is a zone of alteration and mineralization within the Cabo de Gata volcanics.